of inhibitor. At a fivefold excess, **3** inhibited approximately 50% of both thrombin and factor Xa activity; this level of inhibition remained relatively unchanged for more than 20 h.[18] However, under similar conditions, the inhibition curves for **4** with thrombin and factor Xa showed marked reactivation (Figures 2 and 3). These data suggest that the enzyme deacylation rate is slow but real. Experiments in progress with **4** will address the question of reversibility of enzyme acylation and will provide rates of deacylation.

Several aliquots of both α-thrombin and factor Xa inhibited with compound **4** were subjected to photolysis. Irradiation of **4** itself resulted in lactonization of the inhibitor to produce 3-methylcoumarin and *p*-amidinophenol. Since neither the coumarin nor the phenol are good inhibitors of serine proteinases,[26] photolysis of enzyme solutions containing compound **4** effectively removed inhibitor from the system. Enzyme solutions inhibited with low concentrations of **4** (0.6–10 μM) were fully reactivated in less than 1 h of irradiation, but photolysis of samples containing higher inhibitor concentrations (30–97 mM) resulted in only partial reactivation (50–65%) after the same period of irradiation. The longer photolysis periods which would be required to photoisomerize higher concentrations **4** (30–100 mM) were not feasible in presence of enzyme, since all proteinases also absorb energy within the mercury–xenon broad band emission spectrum. Control studies confirmed that prolonged irradiation of α-thrombin or factor Xa did result in decreased enzyme activity.

Although chymotrypsin preferably cleaves peptide bonds at aromatic amino acids (phenylalanine, tryosine, and tryptophan), information on its affinity for **4** was needed to better target future chymotrypsin photoactive inhibitors. The altered specificity of this proteinase can be readily accounted for by an important difference in the amino acid sequences of chymotrypsin and trypsin-like enzymes such as trypsin, thrombin, and factor Xa. In general, trypsin and chymotrypsin accommodate substrates within their active sites in exactly the same manner. However, trypsin contains a key aspartic acid residue which can form a salt bridge with the charged amino acid side chains of lysine or arginine. The formation of these ionic bonds conveys added specificity to trypsin peptide bond hydrolysis. In chymotrypsin, this residue has been replaced by Ser189.[27] Since the pK_a of the serine hydroxyl is normally around 14, this amino acid does not form ionic bonds to charged amino acid side chains. Thus, *p*-amidinophenyl esters such as **4** are not readily recognized by chymotrypsin. The speed and efficiency of all photoreactivation experiments with derivative **4** were limited by the (1) extensive overlap between enzyme and inhibitor absorbance spectra and (2) the intensity of the light source. As noted earlier, the extended periods of broadband irradiation required to lactonize high concentrations of **4** eventually degraded the enzyme. Use of a monochromator tuned to appropriate emission maxima of the source (above the Pyrex cutoff within the range of absorption by **4**) produced insufficient intensities for photoisomerization. Future photolysis experiments performed with a tunable laser should produce sufficiently high intensity light for efficient photolysis at a wavelength absorbed only by the inhibitor. Great efficiency can also be achieved by introducing appropriate substitution into the aromatic ring of **4** to red shift and intensify its absorption maxima.

Acknowledgment. This work was supported by grants from the NIH (HL17921, HL24066, and HL31932). X-ray crystallography was performed by Dr. A. T. McPhail of the Duke University Structure Center.

(26) Yaegashi, T.; Nunomura, S.; Okutome, T.; Nakayama, T.; Kurumi, M.; Sakurai, Y.; Aoyama, T.; Fujii, S. *Chem. Pharm. Bull.* **1984**, *32*, 4466.

(27) Blow, D. M.; Steitz, T. A. *Ann. Rev. Biochem.* **1970**, *39*, 63.

Variable Photon Energy Photoelectron Spectroscopic Studies of Copper Chlorides: An Experimental Probe of Metal–Ligand Bonding and Changes in Electronic Structure on Ionization

Stephen V. Didziulis, Susan L. Cohen, Andrew A. Gewirth, and Edward I. Solomon*

Contribution from the Department of Chemistry, Stanford University, Stanford, California 94305. *Received April 17, 1987*

Abstract: Variable photon energy photoelectron spectra (PES) are reported for the valence band region of cuprous and cupric chlorides for photon energies between 22 and 1253.6 eV. Intensity changes of the PES peaks observed with variation of photon energy are associated with (1) the photoionization cross sections of Cu 3d and Cl 3p atomic orbitals, (2) the Cooper minimum of the Cl 3p orbitals, and (3) resonance effects at the Cu 3p absorption edge. These effects allow a definitive assignment of specific PES features, an experimental estimate of covalent mixing between metal and ligand orbitals for all valence levels, and a quantitative evaluation of relaxation effects on the ionized final states. The intensity changes of the $CuCl_4^{2-}$ PES peaks are found to be dramatically different from those of $CuCl_4^{3-}$, a result of increased covalent mixing in the cupric chlorides. Quantitative analysis of the PES data indicates that in D_{4h} $CuCl_4^{2-}$, the highest energy level, $3b_{1g}$, has 65% Cu 3d character while the antibonding metal levels together have 78% d character. For D_{2d} $CuCl_4^{2-}$, the highest energy level has less covalent mixing than the D_{4h} salt (68% Cu 3d character), while the mixing averaged over all the metal levels increases (76% Cu 3d). The values for the covalent mixing of the highest energy occupied level are in good agreement with the results from other spectroscopic methods, and variable energy PES provides an additional probe of the covalent mixing averaged over all metal and ligand valence levels. The valence band PES spectra of the cupric chlorides also show satellite peaks with significant intensity out of resonance ($\sim$10% of main band intensities) and large resonance enhancement at the Cu 3p $\rightarrow$ 3d absorption edge. These data require large final-state relaxation effects which have been interpreted both in terms of SCF-Xα-SW calculations and a Configuration Interaction model. The relaxation results from a large decrease in metal-centered electron–electron repulsion on ionization which stabilizes the d^8 final state by 6.5 eV. The implications of these results with respect to the redox chemistry of Cu(II) complexes is discussed in terms of covalency effects and metal-centered electron–electron repulsion.

I. Introduction

A major goal of spectroscopic studies on transition metal complexes has been to determine experimentally the bonding interactions between metal ion d orbitals and ligand valence orbitals. One set of complexes which has served as the subject of a large number of experimental and theoretical studies of met-

0002-7863/88/1510-0250$01.50/0

Scheme I

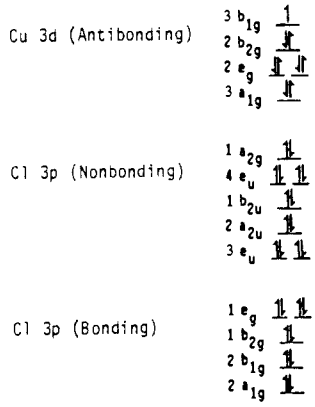

Scheme II

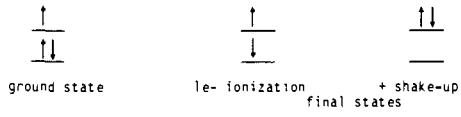

al–ligand bonding is the tetragonal (D_{4h}) $CuCl_4^{2-}$ system.[1] The qualitative energy level diagram of its valence orbitals is given in Scheme I.[2] Studies have focused on the highest energy, half-occupied $3b_{1g}$ level and have shown this orbital to have approximately 61% d character, with the remaining 39% delocalized over the b_{1g} combination of chloride 3p orbitals[3] which is σ bonding to the copper ion.[4] The traditional method employed in this type of study has been electron paramagnetic resonance (EPR) spectroscopy. However, a limitation associated with this physical method is that it probes the bonding interactions of only the highest energy partially occupied orbital(s) of a complex; further, EPR is not useful for diamagnetic or even electron systems.

Limited experimental insight is available for the bonding interactions of the remaining valence levels of $CuCl_4^{2-}$. This insight has derived from polarized optical spectral studies on the ligand field and charge transfer transitions in combination with photoelectron spectral (PES) studies of the valence band of single crystal D_{4h} and D_{2d} distorted $CuCl_4^{2-}$ complexes.[5] The PES spectra were obtained at one photon energy (He II at 40.8 eV), and the peak energies were compared to the absorption spectra to define the σ and π bonding contributions to the charge transfer spectrum. It was understood in this study that differences in relaxation of the final states involved in the two types of transitions (i.e., bound as contrasted to ionized final states) could lead to significant changes in transition energy between the two types of spectroscopies. These relaxation effects derive from the large change in electron–electron repulsion which occurs upon excitation for orbitals frozen in their ground (initial) state distributions. The orbitals will, however, relax so as to change these charge distributions in the final state, reducing the change in electron repulsion. One consequence of final-state relaxation is the presence of weak satellite peaks, which appear in the spectra of Cu(II) complexes at 8-eV deeper binding energy from the main valence band photoemission peaks.[6] As shown in Scheme II, the satellite peak

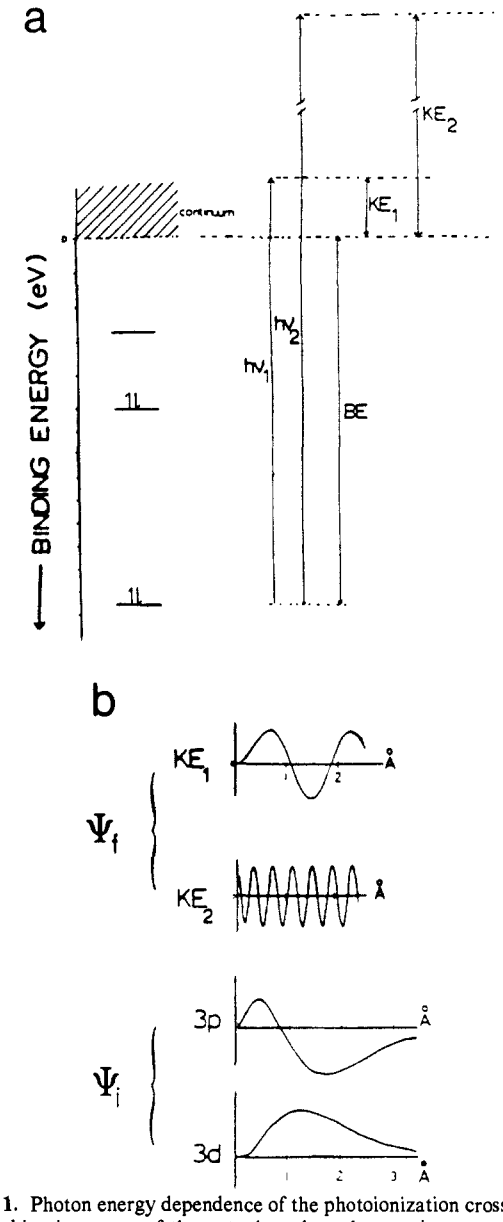

Figure 1. Photon energy dependence of the photoionization cross section: (a) the kinetic energy of the outgoing photoelectron increases with increasing photon energy, $h\nu_2 > h\nu_1$, giving $KE_2 > KE_1$; (b) the different deBroglie wavelengths of the photoelectrons have differing overlap with Cl 3p and Cu 3d atomic orbitals resulting in differing PES peak intensities.

corresponds to the simultaneous ionization plus shake-up of a second electron to generate an excited final state. As this formally corresponds to a two-electron transition, it should have no intensity. However, final-state orbital relaxation overcomes this forbiddeness. Note that the shake-up transitions must involve levels of the same symmetry as the one-electron ionized final states as only these can provide effective relaxation pathways.[7]

In the research presented here, we have extended the earlier PES studies of $CuCl_4^{2-}$ to include the effects of varying photon energy on the valence band PES peak intensities using synchrotron radiation and conventional sources over the energy range of 20 to 1253.6 eV. There are basically three consequences of varying input photon energy on the PES spectrum of a complex: general changes in the orbital photoionization cross sections, Cooper minima in cross sections for specific atomic orbitals, and resonance effects associated with transitions to bound excited states. As the input photon energy is increased from $h\nu_1$ to $h\nu_2$, the kinetic energy of an electron ejected from a level at fixed binding energy (BE) will increase (i.e., $h\nu_i$ = BE + KE_i) as shown in Figure 1a. This

(1) Solomon, E. I. *Comments Inorg. Chem.* **1984**, *3*, 225 and references therein.

(2) In Scheme I only Cu 3d–Cl 3p bonding interactions for D_{4h} $CuCl_4^{2-}$ are considered (see, however, Table III).

(3) (a) Penfield, K. W.; Gewirth, A. A.; Solomon, E. I. *J. Am. Chem. Soc.* **1985**, *107*, 4519. (b) Gewirth, A. A.; Cohen, S. L.; Schugar, H. J.; Solomon, E. I. *Inorg. Chem.* **1987**, *26*, 1133.

(4) It should be noted that while distributing electrons in a wave function among different atomic orbitals is somewhat of a mathematical construct, it is extremely useful in defining effective populations which consistently correlate to a large body of spectroscopic data (vide infra, Table XI).

(5) Desjardins, S. R.; Penfield, K. W.; Cohen, S. L.; Musselman, R. J.; Solomon, E. I. *J. Am. Chem. Soc.* **1983**, *105*, 4590.

(6) (a) Frost, D. C.; Ishitani, A.; McDowell, C. A. *Mol. Phys.* **1972**, *24*, 861. (b) van der Laan, G.; Westra, C.; Haas, C.; Sawatzky, G. A. *Phys. Rev. B* **1981**, *23*, 4369. (c) van der Laan, G. *Solid State Commun.* **1982**, *42*, 165. (d) Thuler, M. R.; Benbow, R. L.; Hurych, Z. *Phys. Rev. B* **1982**, *26*, 669.

(7) Manne, R.; Aberg, T. *Chem. Phys. Lett.* **1970**, *7*, 282.

Scheme III

$$\text{Resonance}: \quad 3p^6\,3d^n \xrightarrow{\text{abs.}} 3p^5\,3d^n\,x^1 \xrightarrow{\text{Auger}} 3p^6\,3d^{n-2}\,x^1$$

$$\text{d ionization}: \quad 3p^6\,3d^n \longrightarrow 3p^6\,3d^{n-1}$$

$$\text{d ionization + shake-up}: \quad 3p^6\,3d^n \longrightarrow 3p^6\,3d^{n-2}\,x^1$$

in turn will change the final-state wave function (ψ_f, Figure 1b) by decreasing the photoelectron wavelength. As the intensity of a PES transition is given by an electronic dipole transition moment of the form $\langle\psi_i|\vec{r}|\psi_f\rangle^2$, it will depend on the final-state wave function and thus the kinetic energy of the ejected electron. The intensity also depends on the initial state, ψ_i, which is determined by the orbital from which the electron is ejected. This dependence on both ψ_i and ψ_f is known as the photoionization cross section and is significantly different for a Cl 3p as compared to a Cu 3d ionization. For an electron ionized from a Cl 3p orbital, the intensity of a PES peak is at a maximum near the ionization threshold and decreases with increasing photon energy.[8] Alternatively, for a Cu 3d ionization, the intensity increases with increasing photon energy reaching a broad delayed maximum at 50 eV.[8,9] This delayed maximum results from the centrifugal barrier in the radial Schrodinger equation which is proportional to $-l(l+1)/r^2$.[9]

An important, additional feature of the Cl 3p atomic photoionization cross section is a local intensity minimum in the photon energy region of 50 eV. This Cooper minimum results from the node in the radial wave function of the 3p orbital as shown in Figure 1b.[10] The change in phase of ψ_i results in cancellation of the electron dipole transition moment to the ψ_f associated with a photon energy of ~50 eV (approximately KE_1 in Figure 1). As the photon energy increases, the wavelength of ψ_f decreases and cancellation no longer occurs. The presence of the Cl 3p Cooper minimum near the same photon energy as the Cu 3d intensity maximum results in a very small relative 3p cross section in this photon energy regime, an important fact used in this study.

The third contribution to PES peak intensity changes with variation in photon energy is a resonance interaction with a transition to a bound state. For 3d transition metal complexes, changes in valence band PES peak intensities are observed at the metal 3p absorption edge. The PES resonance mechanism has been defined by Davis and is given in Scheme III.[11] At photon energies corresponding to the absorption edge, a metal 3p electron is excited to a metal-centered orbital, x. This intermediate state then decays via an Auger process whereby a 3d electron fills the 3p hole and a second 3d electron is ejected. This Auger process involves a Super–Coster–Kronig transition (SCK)[12] in which both the initial and final state holes reside in the same principal quantum shell ($n = 3$). The SCK transition has a high probability due to the localized nature and larger repulsion of d electrons. In Scheme III, if x is a d orbital then the final state reached by excitation at the metal 3p edge is the same as that obtained from direct d photoemission, and the two channels of intensity produce resonance and interference effects. If x is not a d orbital, then resonance effects should be observed in shake-up satellites involving d ionization plus d → x excitation.

In section III we present the variable energy photoelectron spectra of the valence band region of CuCl and of three $CuCl_4^{2-}$ compounds focusing particularly on photon energies near the Cl 3p Cooper minimum and at the Cu 3p absorption edge. Cuprous chloride, with a tetrahedral Cu(I) site, is included in this study as a reference compound as the spectral changes are relatively straightforward based on the limited mixing present between the Cu 3d and Cl 3p orbitals and the fact that the d^{10} ground-state configuration precludes 3p → 3d transitions at the copper 3p absorption edge. Two of the $CuCl_4^{2-}$ compounds studied are tetragonal with different counterions (potassium[13] and methylammonium), while the third has a D_{2d} distorted tetrahedral $CuCl_4^{2-}$ site (Cs_2CuCl_4). In section IV.A, the striking differences which are observed in the variable energy PES intensities of the valence bands in the $CuCl_4^{2-}$ compounds relative to CuCl are interpreted in terms of increased covalent mixing between Cu 3d and Cl 3p orbitals in the D_{4h} $CuCl_4^{2-}$ complex and correlated to the results of Xα–SW calculations on the ground state of this complex. In section IV.B, the variable energy PES intensities of the valence band satellites are analyzed in terms of final-state relaxation. The data in combination with Xα–SW calculations, which include relaxation and shake-up, are used to (1) assign the satellite peaks to specific transitions, (2) probe the nature of the relaxation process which produces the resonance intensity, and (3) consider the nonresonance intensity redistribution for the satellite states. In section IV.C, a Configurational Interaction (CI) model which has been developed by Hubbard et al.[14] and applied to PES by Sawatzky,[6b] Davis,[11] and van der Laan[6c] is presented and used in conjunction with our PES data to obtain an additional experimental estimate of covalent mixing and relaxation effects in D_{4h} $CuCl_4^{2-}$. The results of this CI model are compared with those from the Xα–SW calculations and used to gain further insight into the resonance intensity profiles. Finally, in section IV.D, the results for D_{2d} $CuCl_4^{2-}$ are compared quantitatively with those for D_{4h} $CuCl_4^{2-}$ and used to probe experimentally the differences in bonding associated with the distortion from tetragonal to tetrahedral geometry.

II. Experimental Section

Cuprous chloride, a wide band gap semiconductor with the zinc blende structure,[15] was obtained as a large polycrystal (20 × 5 × 2 mm) from Professor T. Geballe, Department of Applied Physics, Stanford University. Single crystals of the three $CuCl_4^{2-}$ compounds (Cs_2CuCl_4,[16] $(CH_3NH_3)_2CuCl_4$,[17] and $KCuCl_3$[18]) were prepared by established methods. The crystal structures of Cs_2CuCl_4[19] and $KCuCl_3$[20] are known while a structure of $(CH_3NH_3)_2CuCl_4$ has not been solved but it is isostructural with $(C_2H_5NH_3)_2CuCl_4$.[17a]

All XPS and UPS spectra were taken in a Vacuum Generators ESCALAB Mk II system employing a differentially pumped twin anode X-ray source (Mg Kα, 1253.6 eV, and Al Kα, 1486.6 eV) and a differentially pumped, windowless dc discharge source run with He gas (21.2, 40.8, and 48.4 eV) or Ne gas (26.8 eV). The ESCALAB system is equipped with a hemispherical analyzer (150° spherical sector, radius = 150 mm) with a 6° cone of acceptance and single channel detection with a channeltron electron multiplier. Other facilities available include Auger electron spectroscopy, a charge neutralizing electron flood gun, a Varian argon ion sputter gun, sample manipulator with heating and cooling capability, a sample preparation chamber, and a fast entry air lock allowing rapid introduction of samples into the vacuum system. The base pressure of the system was typically $<5 \times 10^{-11}$ torr while the pressure during operation with the discharge lamp was 2×10^{-10} torr.

Spectra at all other photon energies were taken using synchrotron radiation at the Stanford Synchrotron Radiation Laboratory (SSRL) on three different SPEAR beam lines using two different ultra-high-vacuum (UHV) systems. The low photon energy data (18–30 eV) were obtained on beam line I-2 which employs a Seya Namioka monochromator with energy resolution of better than 200 meV using a 1200-lines/mm grating and 300-μm inlet and outlet slits.[21] The UHV system used in these

(8) Yeh, J. J.; Lindau, I. *At. Data Nucl. Data Tables* **1985**, *32*, 1.
(9) (a) Fano, U.; Cooper, J. W. *Rev. Mod. Phys.* **1968**, *40*, 441. (b) Manson, S. T.; Cooper, J. W. *Phys. Rev.* **1968**, *165*, 126. (c) Eastman, D. E.; Kusnietz, M. *J. Appl. Phys.* **1971**, *42*, 1396.
(10) Cooper, J. W. *Phys. Rev.* **1962**, *128*, 681.
(11) Davis, L. C. *Phys. Rev. B* **1982**, *25*, 2912.
(12) Davis, L. C.; Feldkamp, L. A. *Phys. Rev. B* **1981**, *23*, 6239.
(13) The potassium salt exists as a dimer, $Cu_2Cl_6^{2-}$, but has no significant $CuCl_4^{2-}$ PES spectral differences from the methyl ammonium salt.
(14) Hubbard, J.; Rimmer, D. E.; Hopgood, F. R. A. *Proc. Phys. Soc.* **1966**, *88*, 13.
(15) (a) Wyckoff, R. W. G. *Crystal Structures*; R. E. Krieger Publishing Co.: Malabar, Florida, 1982. (b) Nikitine, S. *Prog. Semicond.* **1962**, *6*, 271.
(16) Sharnoff, M.; Reiman, C. *J. Chem. Phys.* **1964**, *40*, 3406.
(17) (a) Steadman, J. P.; Willett, R. D. *Inorg. Chim. Acta* **1970**, *4*, 367. (b) Arend, H.; Huber, W.; Mischgofsky, F. H.; Richter-van Leeuwen, G. K. *J. Cryst. Growth* **1978**, *43*, 213. (c) Willett, R. D. *J. Chem. Phys.* **1964**, *41*, 2243.
(18) Desjardins, S. R.; Wilcox, D. E.; Musselman, R. L.; Solomon, E. I. *Inorg. Chem.* **1987**, *26*, 288.
(19) McGinnety, J. A. *J. Am. Chem. Soc.* **1972**, *94*, 8406.
(20) Willett, R. D.; Dwiggens, C., Jr.; Kruh, R. F.; Rundle, R. E. *J. Chem. Phys.* **1963**, *38*, 2429.

experiments was an ion pumped Vacuum Generators (VG) chamber (ADES-400) employing an angle-resolved hemispherical analyzer with a 2° acceptance angle, single channel detection, and a base pressure of $<1 \times 10^{-10}$ torr. The system was equipped with a manipulator capable of x,y,z translation and rotation in two planes as well as an electron flood gun. Samples were introduced into the chamber with a magnetically coupled transfer arm after cleaning in a small, independently pumped sample introduction/preparation chamber.

Higher photon energy data (25–200 eV) data were obtained on beam lines I-1 and III-1, both of which employ grasshopper monochromators.[22] The energy resolution of beam line I-1 (1200-lines/mm grating, 15-μm slits) ranges from 30 meV at 65 eV to 180 meV at 150 eV. Beam line III-1 is equipped with interchangeable gratings (600 and 1200 lines/mm), variable slits for constant photon energy resolution, and transmission filters to minimize higher order light contributions.[22c] An ion-pumped Perkin-Elmer (Physical Electronics) chamber with a double-pass cylindrical mirror analyzer (CMA) with single channel detection was used. The chamber also contained an argon ion sputter gun, flood gun, sample manipulator with x,y,z translation and rotation, and the same sample preparation chamber/transfer arm arrangement. The variable slits on beam line III-1 were adjusted to maintain a constant photon energy resolution of 200 meV.[22c] The resolution of the analyzers used in all of these experiments was kept at better than 200 meV such that the spectral resolution is limited by charging effects inherent with insulating samples and the photon energy resolution.

Sample cleaning was performed by a variety of methods both external and internal to the UHV chambers. All samples except the $(CH_3NH_3)_2CuCl_4$ crystals were initially polished in a nitrogen atmosphere with 9-μ grit Al_2O_3 plastic lapping sheets (Imperial Lapping Film, 3M Co.) and quickly moved into the vacuum system. Further cleaning in a vacuum was performed by mechanical "polishing" with 100–200-μ grit diamond wheels mounted on rotary feedthroughs in the sample preparation chambers. The CuCl sample was also sputtered with Ar ions at 500 V, an accelerating potential which caused no reduction of the Cu(I) ions. The layered $(CH_3NH_3)_2CuCl_4$ samples were prepared by cleavage with Scotch tape in a nitrogen atmosphere followed by rapid introduction to UHV. Ion sputtering and Auger could not be used on the cupric salts as these techniques cause sample damage and reduce the Cu(II) ions. Surface cleanliness was monitored by core level XPS or by the ability to resolve valence band PES features at low photon energies, where the cross sections of common contaminants are quite high. Samples were cooled to 160 K and low X-ray powers (less than 90 W) were used during XPS collection to minimize damage. Further cleaning was administered as necessary.

The insulating cupric salts required the use of the low-energy electron flood gun to neutralize surface charging during data collection. Generally, 10–100 nA of 0–2-eV electrons was needed for effective charge neutralization. All spectra were signal averaged, with 40–60 scans needed for satisfactory signal to noise. Data on the insulators were collected in 10 scan sets to minimize the effects of differential charging with time. These sets were then added together after compensating for any kinetic energy shifts (usually $\leq$0.2 eV). All spectra taken at SSRL were normalized to the total monochromatic photon flux by a monitor consisting of a gold-coated stainless steel mesh located in the path of the incident radiation with photoemitted electrons detected by a total yield channeltron detector.[23]

Constant initial state (CIS) spectra were obtained by scanning both the photon energy and analyzed kinetic energy such that the intensity of a peak at constant binding energy was determined as a function of photon energy. The slit widths were adjusted such that the photon energy resolution was always better than 200 meV. The pass energy of the analyzer was increased to 50 eV to increase the count rate and minimize the number of scans. Constant final state (CFS) spectra were obtained by scanning the photon energy while analyzing electrons in the secondary electron peak at 8-eV kinetic energy with the pass energy at 50 eV (partial yield detection). These spectra are analogous to absorption spectra.[24]

Standard versions of the Xα-SW code were used to calculate the electronic structure of both D_{4h} and D_{2d} geometries of $CuCl_4^{2-}$. For D_{4h} $CuCl_4^{2-}$, the average (2.265 Å) of the Cu–Cl bond lengths in *N*-methylphenethylammonium copper(II) chloride[25] was used. For the D_{2d} geometry, the structural data for Cs_2CuCl_4[19] were used: the averages of all Cu–Cl bond lengths (2.230 Å), the two small Cl–Cu–Cl angles (100.7°), and the two large Cl–Cu–Cl angles (129.2°). The α values of Schwarz[26] were used in the atomic regions, while l values of 7, 5, and 3 were used for the outer-sphere, Cu, and Cl centers, respectively. Overlapping sphere radii were determined by fitting the ground-state wave function to the experimental g values[3b,27,28] with tangential outer spheres. For D_{4h} $CuCl_4^{2-}$ the Cu radius was 2.97 bohr while 2.54 bohr was used

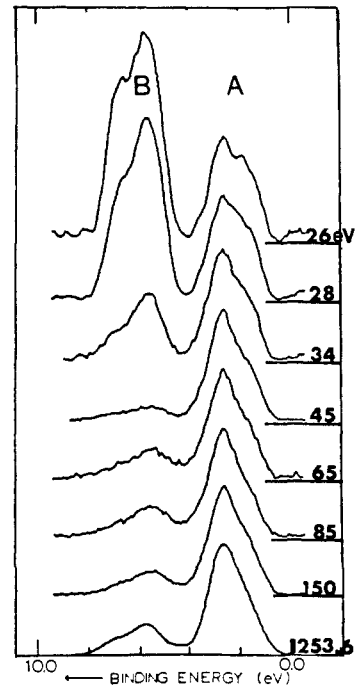

Figure 2. Variable photon energy valence band photoelectron spectra of CuCl referenced to $E_F = 0$ eV. All spectra are normalized to the height of band A.

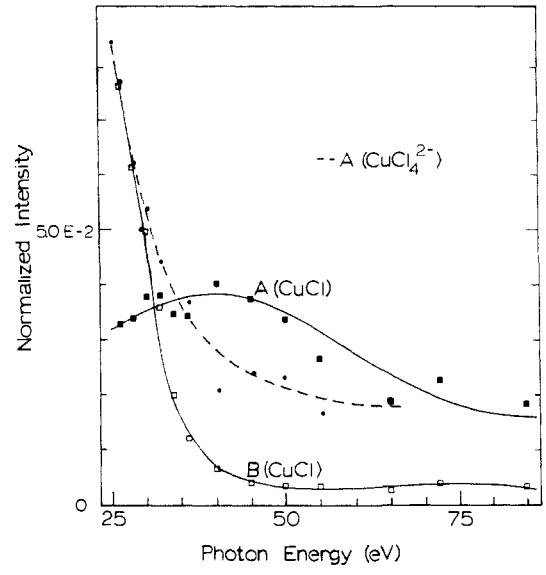

Figure 3. Photon energy dependence of the absolute intensities of peaks A (■) and B (□) in the valence band spectra of CuCl. The intensity of peak A from D_{2d} $CuCl_4^{2-}$ (●) is also plotted. All intensities have been normalized to the incident photon flux.

(21) Saile, V. *Nucl. Instrum. Methods* **1978**, *152*, 59.
(22) (a) Brown, F. C.; Bachrach, R. Z.; Lien, N. *Nucl. Instrum. Methods* **1978**, *152*, 73. (b) Stohr, J. *Instruction Manual for the New Grasshopper Monochromator*, Stanford Synchrotron Radiation Laboratory, Stanford CA, 1980. (c) Pate, B. B. Ph.D. Thesis, Stanford University, 1984.
(23) (a) Stohr, J.; Jaeger, R.; Brennan, S. *Surf. Sci.* **1982**, *117*, 503. (b) Hecht, M. Ph.D. Thesis, Stanford University, 1982.
(24) Lindau, H. I.; Spicer, W. E. *Synchrotron Radiation Research*; Winick, H., Doniach, S., Eds.; Plenum Press: New York, 1980; Chapter 6, pp 167, 168.
(25) Harlow, R. L.; Wells, W. J., III; Watt, G. W.; Simonsen, S. H. *Inorg. Chem.* **1974**, *13*, 2106.
(26) Schwarz, K. *Phys. Rev. B* **1972**, *5*, 2266.
(27) Gewirth, A. A. Ph.D. Thesis, Stanford University, 1987.
(28) (a) Solomon, E. I.; Gewirth, A. A.; Cohen, S. L. *Understanding Molecular Properties*; Hansen, A. E., Avery, J., Dahl, J. P., Eds.; D. Reidel: Dordrecht, 1987; pp 27–68. (b) Bencini, A.; Gatteschi, D. *J. Am. Chem. Soc.* **1983**, *105*, 5535.

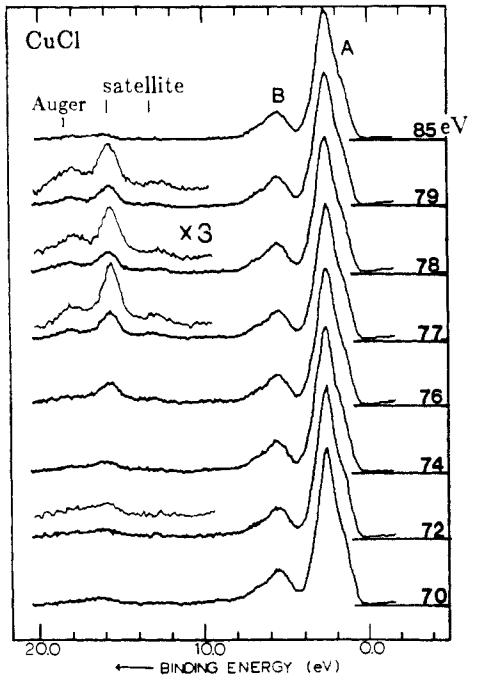

Figure 4. Resonant photoemission spectra of CuCl at the Cu 3p absorption edge. The region from 10 to 20 eV is also given at higher sensitivity to show the multielectron satellite and the $M_{2,3}M_{4,5}M_{4,5}$ Auger peak.

for Cl. In D_{2d} $CuCl_4^{2-}$, the corresponding radii were 3.11 and 2.49 bohr, respectively.

III. Results

A. CuCl. The variable photon energy valence band photoelectron spectra of CuCl are shown in Figure 2. The valence region is composed of two major bands, A and B, each of which is split into two components with features at binding energies of 1.7 and 2.7 eV, and at 5.5 and 6.8 eV, respectively, relative to the Fermi level. At low photon energies, the deeper binding energy band B is the more intense. As the input photon energy increases, this peak drops dramatically in intensity relative to band A reaching a minimum near 45 eV photon energy, which corresponds to the Cl 3p Cooper minimum. The relative intensity of band B then increases as the photon energy increases to 1253.6 eV. The absolute intensity of these two main features as a function of photon energy is given in Figure 3; band A increases in intensity to a delayed maximum at approximately 40 eV while band B is intense at low photon energy and reaches a minimum in intensity near 50 eV. This qualitative behavior corresponds with that calculated for 3d and 3p atomic photoionization cross sections as described in the Introduction and clearly identifies band A as ionization from the Cu 3d orbitals while band B is attributed to Cl 3p ionization. This assignment is consistent with the previous studies by Goldmann et al. using resonance lamp radiation.[29]

Three peaks in the CuCl valence band spectrum near 16-eV binding energy are enhanced in intensity as the photon energy is scanned through the Cu 3p absorption edge between 74 and 80 eV (Figure 4). The peaks at 13.2 and 15.7 eV are satellite peaks while the peak at 18.6 eV has been assigned as $M_{2,3}M_{4,5}M_{4,5}$ Auger electron emission.[30] The intensities of the satellite peaks approach zero away from resonance photon energies. The CFS edge spectrum for CuCl is shown in Figure 5, with the Cu 3p → 4s transition observed at 77–80 eV. The CIS intensity profile of the satellite (Figure 5) is similar to the CFS spectrum, with intensity maxima at 76.9 and 78.9 eV indicating that the satellites are resonance enhanced at the Cu 3p → 4s absorption edge. The 2-eV splitting of the satellite intensity maxima corresponds to the spin–orbit splitting of the excited Cu(I) $3p^54s^1$ configuration. A CIS spectrum of the Cu 3d band A exhibits only a broad, weak dip in intensity in this energy region, and no intensity change is observed in the Cl 3p band B. These resonant photoemission results are very similar to those obtained by Ishii et al.[30] The energies of the CuCl features are summarized in Table I.

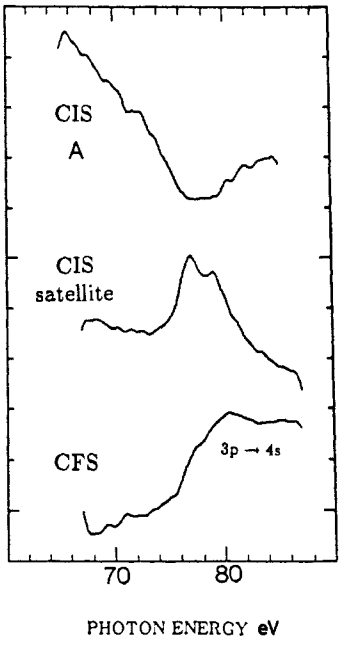

Figure 5. Constant initial state intensity profiles of band A and the satellite peak of CuCl showing resonance effects from 76 to 80 eV photon energy. The constant final-state (CFS) spectrum is also included.

Table I. Copper Chloride PES Peak and Resonance Energies

A. Peak Binding Energies (eV)

	A	B	satellite
D_{4h} $CuCl_4^{2-}$	3.6	5.4	10.2, 12.5
D_{2d} $CuCl_4^{2-}$	3.6	5.4	9.8, 12.0
CuCl	1.7, 2.7	5.5, 6.8	13.2, 15.7

B. Cu 3p Edge Features—Photon Energy (eV)[a]

	CIS A	CIS satellite	CFS	assignment
D_{4h} $CuCl_4^{2-}$	73.7, 76.3	73.9, 76.2	74.1, 76.1	3p → 3d
			80.3, 81.7	3p → 4s
CuCl	77, 79	76.9, 78.7	77.1, 80.3	3p → 4s

[a] Resonance data for D_{2d} $CuCl_4^{2-}$ have not been included as interference from Cs photoemission features prevents an accurate determination of resonant energies. The Cs 4p absorption edge occurs near 75 eV, Cs 4p photoemission from second-order light overlaps peaks A and B, and the Cs 5p peaks overlap the valence band satellite.

B. $CuCl_4^{2-}$. (i) Spectra. Valence band spectra of the three d^9 $CuCl_4^{2-}$ complexes were obtained over the photon energy range of 22–1253.6 eV. The intrinsic $CuCl_4^{2-}$ valence band photoemission features were distinguished from those of the counterion by comparison to photoemission spectra of counterion salts and by the photon energy dependence of the counterion peak intensities. The binding energies for these insulating samples are referenced to the Cu $2p_{3/2}$ level at 933.9 eV for a Cu(II) ion.

Selected variable energy valence band spectra of $(CH_3NH_3)_2CuCl_4$ are shown in Figure 6a. The peaks between 8 and 14 eV binding energy (labeled with asterisks) are attributed to $(CH_3NH_3)^+$ counterion photoemission based on their photon energy dependence (the decreasing intensity with increasing photon energy indicates 2p photoemission), and by comparison with the spectra of gas-phase CH_3NH_2 and solid $C_2H_5NH_3Cl$.[31] The C 2s emission from $CH_3NH_3^+$ (16.6 eV) overlaps with the Cl 3s

(29) Goldmann, A.; Tejeda, J.; Shevchik, N. J.; Cardona, M. *Phys. Rev. B* **1974**, *10*, 4388.
(30) Ishii, T.; Taniguchi, M.; Kakizaki, A.; Naito, N.; Sugawara, H.; Nagakura, I. *Phys. Rev. B* **1986**, *33*, 5664.
(31) (a) Ogata, H.; Onizuka, H.; Nihei, Y.; Kamada, H. *Bull. Chem. Soc. Jpn.* **1973**, *46*, 3036. (b) Potts, A. W.; Williams, T. A.; Price, W. C. *Discuss. Faraday Soc.* **1972**, *54*, 104.

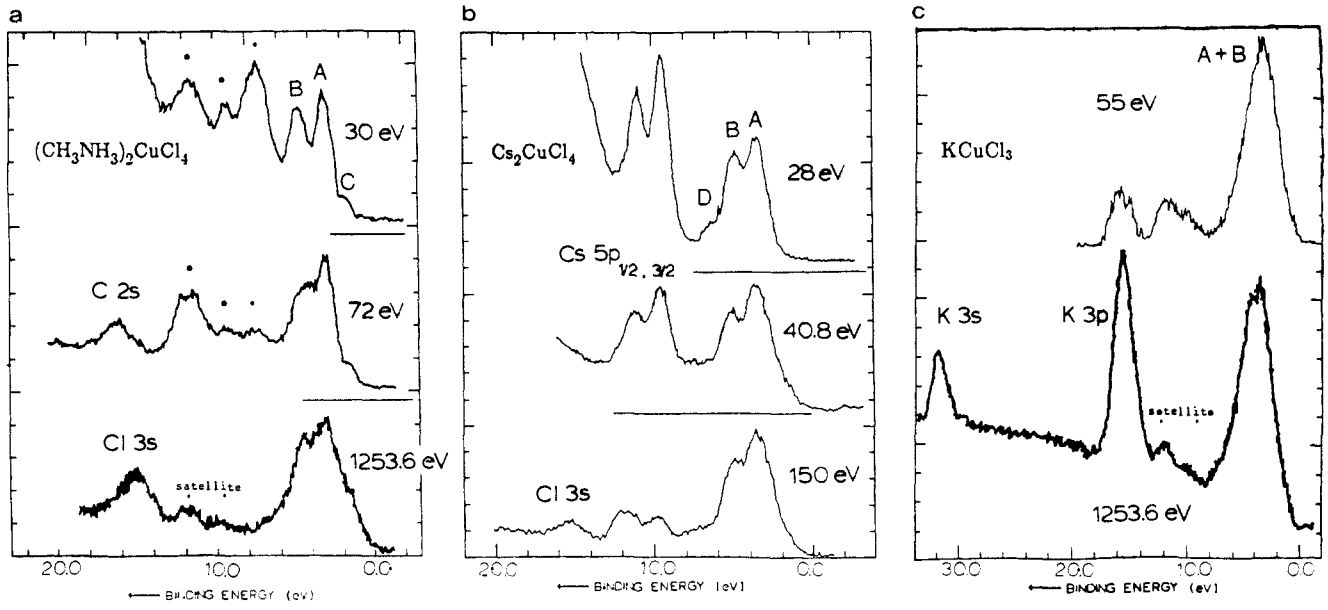

Figure 6. Selected variable photon energy valence band spectra of $CuCl_4^{2-}$ used to determine counterion ionizations for (a) $(CH_3NH_3)_2CuCl_4$ (* = $CH_3NH_3^+$ contribution), (b) Cu_2CuCl_4, and (c) $KCuCl_3$. Peaks labeled A, B, and C are attributed to $CuCl_4^{2-}$ photoemission.

emission (15.3 eV) of the $CuCl_4^{2-}$ unit. The C 2s cross section dominates at 72 eV while the Cl 3s is dominant at 1253.6 eV, causing the shift of this peak to lower binding energy as the photon energy increases. The bands labeled A, B, and C between 2 and 6 eV binding energy are most intense relative to the $CH_3NH_3^+$ features at 1253.6 eV, and are assigned as emission from the D_{4h} $CuCl_4^{2-}$ complex.

Selected spectra of the D_{2d} Cs_2CuCl_4 complex are given in Figure 6b. The two intense peaks at binding energies between 3 and 6 eV (labeled A and B) are observed at all photon energies and are attributed to emission from the $CuCl_4^{2-}$ complex. The two peaks at 9.5 and 11.6 eV are attributed to Cs $5p_{3/2,1/2}$ emission. These peaks are intense at low and high photon energies (XPS spectrum not shown) but are weak at 150 eV due to the significant decrease in the 5p cross section at this photon energy.[8] This assignment is also consistent with the UPS spectra of CsCl.[32] The Cl 3s peak is observed at 15.3 eV in the 150-eV spectrum.[33]

Spectra of $KCuCl_3$ taken at photon energies of 55 and 1253.6 eV are shown in Figure 6c. As in the D_{4h} and D_{2d} monomers, the lowest binding energy features, which overlap more in this salt due to charging effects (composite band A + B), are assigned as $CuCl_4^{2-}$ emission. The K 3p and K 3s emissions are observed at 15.5 and 31.8 eV, respectively, consistent with their binding energies in KCl. The dramatic intensity decrease of the 15.5-eV peak in the 55-eV spectrum is consistent with the presence of the K 3p Cooper minimum near 50 eV.

In addition to the main $CuCl_4^{2-}$ features (A and B) observed in the valence band spectra of all three chlorocuprate salts, two satellite peaks are observed in the binding energy region of 10–13 eV in selected spectra. These satellite peaks are unobscured by counterion emission in $KCuCl_3$ spectra and appear at binding energies of 10.1 and 12.5 eV (Figure 6c). In $(CH_3NH_3)_2CuCl_4$ (Figure 6a), the $CH_3NH_3^+$ emission is weak relative to the $CuCl_4^{2-}$ emission at $h\nu$ = 1253.6 eV, allowing the satellites at 10.1 and 12.5 eV to be observed. In Cs_2CuCl_4 (Figure 6b) the satellite peaks overlap with the Cs $5p_{1/2}$ emission causing apparent broadening and shifting of the Cs $5p_{1/2}$ peak and a change in the intensity ratio of the $5p_{3/2}$ to $5p_{1/2}$ peaks at 150 eV. Unfortunately this overlap precludes accurate intensity measurement of the satellite peaks for this complex. The energies of the main and satellite PES peaks of $CuCl_4^{2-}$ in the three compounds studied are summarized in Table I.A.

(ii) Photoionization Cross Sections. We now concentrate on the photon energy dependence of the intensities of $CuCl_4^{2-}$ main bands A and B. The Cs_2CuCl_4 data for photon energies from 22 to 1253.6 eV are shown in Figure 7a. The most distinct change with photon energy is the variation in the intensity ratio of bands A and B. As the photon energy increases from 22 to 48.4 eV, which is approximately the Cl 3p Cooper minimum, the intensity of band B decreases relative to band A. Band B then increases again in intensity at 1253.6 eV. Additionally, the two peaks have a photon energy dependent change in their apparent energy splitting. The 1.0-eV separation of A and B at $h\nu$ = 22 eV increases to 1.5 and 1.8 eV at photon energies of 30 and 48.4 eV, respectively, with peak B apparently shifting to deeper binding energy. Simultaneously, there is a decrease in intensity in the region between peaks A and B. The shift of band B and the decrease in intensity in the region between the bands indicates that a third peak, labeled N, contributes to the valence band emission with a binding energy about halfway between the binding energies of peaks A and B. The photon energy dependence of N is different from either A or B in that it is intense at low photon energies but then exhibits a larger decrease in intensity than either bands A or B at 50 eV.

The variable energy valence band PES spectra of D_{4h} $CuCl_4^{2-}$ in Figure 7b are quite similar to those described above for D_{2d} $CuCl_4^{2-}$. Clearly, band B decreases in intensity relative to A as the photon energy increases from 22 to the Cl 3p Cooper minimum at 48.4 eV, and then increases in the XPS spectrum. Although the shift of band B to deeper binding energy is less dramatic in this complex than in D_{2d} $CuCl_4^{2-}$, a decrease in intensity in the region between bands A and B is evident as the photon energy increases to 48.4 eV, again showing the presence of a band N. The relative peak intensities for all $CuCl_4^{2-}$ valence spectra were determined by a fit of two Gaussian bands to features A and B.[34] The experimental A/B intensity ratios for D_{4h} $CuCl_4^{2-}$ at photon energies of 22, 48.4, and 1253.6 eV are given in Table II.A. A fourth peak, located on the low binding energy side of band A (labeled C in Figure 7), is present only in the D_{4h} salt and exhibits an intensity dependence on photon energy similar to that of band A.

(32) (a) Poole, R. T.; Jenkin, J. G.; Liesegang, J.; Leckey, R. C. G. *Phys. Rev. B* **1975**, *11*, 5179. (b) Poole, R. T.; Jenkin, J. G.; Leckey, R. C. G.; Liesegang, J. *Chem. Phys. Lett.* **1973**, *22*, 101. (c) Goodman, T. D.; Allen, J. D., Jr.; Cusachs, L. C.; Schweitzer, G. K. *J. Electron Spectrosc. Relat. Phenom.* **1974**, *3*, 289.

(33) There is also a small peak labeled D in Figure 6 which is intense only at low energies and which is attributed to an impurity since it is not observed in all samples of the same material.

(34) A three-peak fit was not attempted because of uncertainty in the binding energy position of band N which is, therefore, treated as contributing equally to peaks A and B. An additional small peak corresponding to band C was included to fit the data in Figure 9b to estimate its resonance behavior.

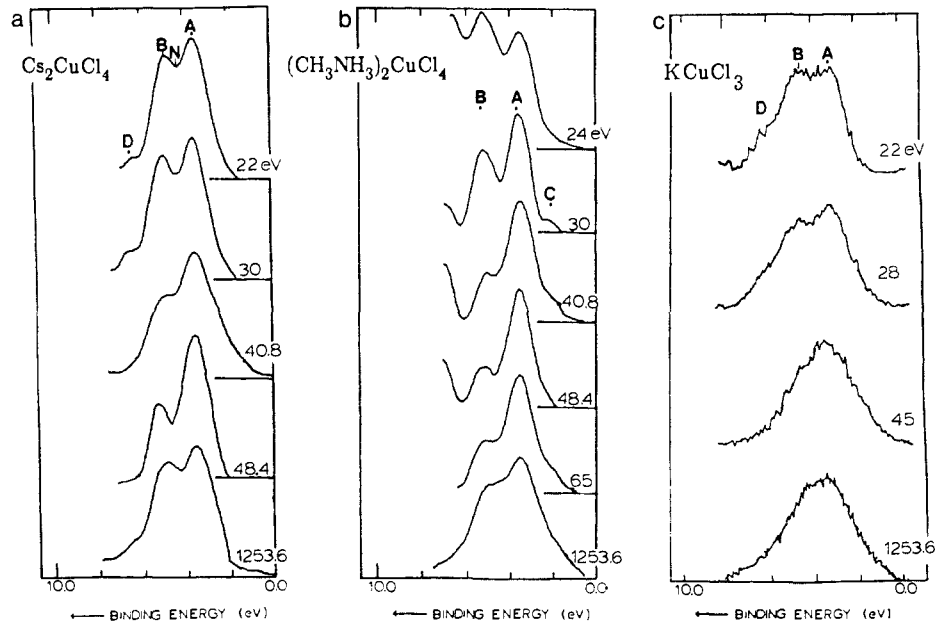

Figure 7. Variable photon energy valence band spectra of (a) Cs_2CuCl_4, (b) $(CH_3NH_3)_2CuCl_4$, and (c) $KCuCl_3$ normalized to the height of the most intense feature.

Table II. D_{4h} $CuCl_4^{2-}$ PES Peak Intensity Ratios

	22 eV	48.4 eV	1253.6 eV
A. Experimental[34]			
A/B	1.1	3.2	1.3
satellite/(A + B)		0.09	0.07

	σ_L = 0.20	0.012	0.00	0.035
B. Xα–SW Calculation (σ_{3d} = 0.10)				
1. Ligand Field				
$\frac{A + 0.5N}{B + 0.5N}$	0.68	4.82	∞	1.92
2. Covalent Ground State				
$\frac{A + 0.5N}{B + 0.5N}$	0.76	2.27	3.88	1.44
$\frac{\text{satellite}}{A + B + N}$	0.00	0.00	0.00	0.00
3. Relaxed Final State				
$\frac{A + 0.5N}{B + 0.5N}$	1.05	2.09	2.84	1.60
$\frac{\text{satellite}}{A + B + N}$	0.03	0.05	0.05	0.04
C. CI Calculation (σ_{3d} = 0.10)[a]				
1. Frozen Orbital (U = 0.0)				
$\frac{A + 0.5N}{B + 0.5N}$	0.77	2.28	3.87	1.45
$\frac{\text{satellite}}{A + B + N}$	0.00	0.00	0.00	0.00
2. Relaxed Final State (U = 6.5)				
$\frac{A + 0.5N}{B + 0.5N}$	1.25	0.55	0.32	0.81
$\frac{\text{satellite}}{A + B + N}$	0.07	0.38	0.55	0.24

[a] For the CI calculation, the wave functions used to determine each peak intensity are grouped together in Table IX. For example, the intensities for all ψ_1 states were summed to form band A.

$KCuCl_3$ spectra acquired at several different photon energies are shown in Figure 7c. At 22 and 28 eV there are clearly two peaks. The general photon energy depenence of the bands A and B is the same as for D_{4h} and D_{2d} $CuCl_4^{2-}$ as band B decreases significantly in relative intensity at 45-eV photon energy. The peaks are broader in the $KCuCl_3$ spectra due to charging effects and the changes are not as distinct. The intensity of band B is weaker in the XPS spectrum of $KCuCl_3$ than in either of the other two complexes consistent with the Cl/Cu stoichiometry.

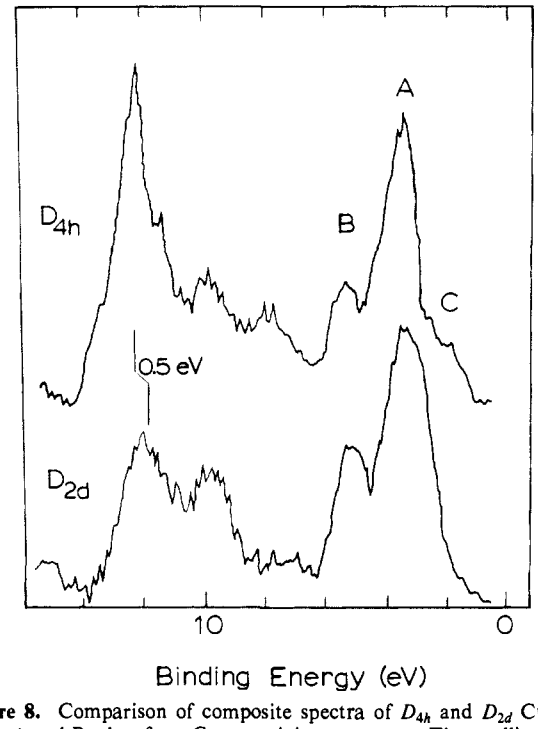

Figure 8. Comparison of composite spectra of D_{4h} and D_{2d} $CuCl_4^{2-}$: peaks A and B taken from Cooper minimum spectra. The satellite region is at the maximum resonance enhancement (73.5–74 eV).

In Figure 3, the absolute intensity of band A for Cs_2CuCl_4 is plotted as a function of photon energy with the analogous data for the Cu 3d band and the Cl 3p band of CuCl. The emission from peak A in the Cu(II) salt clearly differs from the Cu 3d band A of the Cu(I) compound in that it is quite strong at low photon energies and decreases by a factor of 4 as the photon energy increases to 50 eV.

Finally, there are two quantitative differences between the valence band spectra of D_{2d} and D_{4h} $CuCl_4^{2-}$ shown in the composite spectra of Figure 8. First, in spectra taken with photon energies of 40–50 eV, the intensity of band B is greater relative

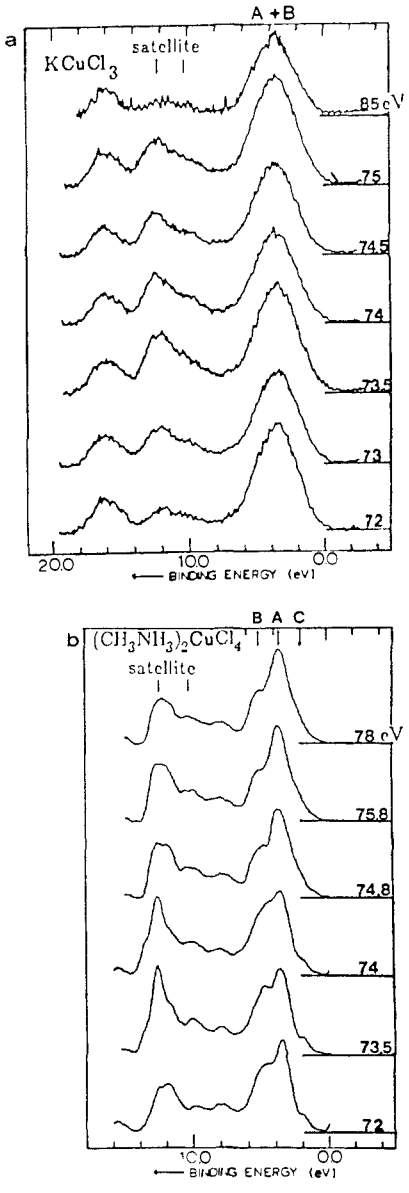

Figure 9. Resonant photoemission spectra of (a) $KCuCl_3$ and (b) $(CH_3NH_3)_2CuCl_4$ taken through the Cu 3p absorption edge.

to band A for the distorted tetrahedral $CuCl_4^{2-}$ molecule. Second, band C is present as a low binding energy shoulder in D_{4h} but not D_{2d} $CuCl_4^{2-}$.

(iii) Resonance Photoemission. The remaining sets of data focus on resonant photoemission effects observed over a limited photon energy region between 72 and 85 eV, near the Cu 3p absorption edge. The valence band photoemission spectra of $KCuCl_3$ over this energy region are shown in Figure 9a. At 72 eV, the satellite peaks have a total intensity equal to 12% of the main valence band peak (A + B). As the photon energy increases, the satellite peaks increase in intensity by a factor of 3 to a maximum at 73.5-eV photon energy and then decrease to their original off-resonance intensity by 85 eV. Concurrent with the changes in satellite intensity at 73.5-eV photon energy, the band A + B has decreased in intensity by 13% of its off-resonance intensity. No resonance effects are observed in the Cl 3s/K 3p peaks at 15.5-eV binding energy.

The CFS absorption spectrum for $KCuCl_3$, shown in Figure 10a, has two sets of peaks, one at 74.1, 76.1 and a second set at 80.3, 81.7 eV, which are assigned as 3p → 3d and 3p → 4s transitions, respectively.[35] The 1.4–2.0-eV separation of the two components of each absorption edge transition is due to the

(35) Butcher, K. D.; Didziulis, S. V.; Cohen, S. L.; Gewirth, A. A.; Solomon, E. I., to be published.

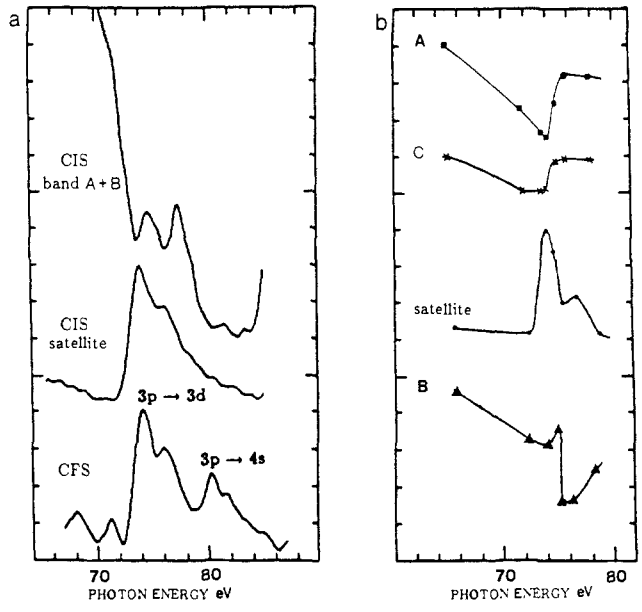

Figure 10. (a) CIS intensity profiles of peak A and B and the satellite peak of $KCuCl_3$ compared to the CFS spectrum. (b) Intensity profiles of valence band features of $(CH_3NH_3)_2CuCl_4$ as determined by Gaussian resolution of valence band spectra.

spin–orbit splitting of the Cu 3p core hole. The total integrated intensity of the Cu 3p → 3d edge features is 4.6 times greater than that of the Cu 3p → 4s absorption edge features. CIS intensity profiles of the individual photoemission peaks in the energy region of the 3p absorption edge are also included in Figure 10a. The satellite CIS profile in $KCuCl_3$ has two peaks at 73.7 and 76.3 eV while band A + B has two minima in intensity at the same photon energies. It is important to note that for both the satellite and main band, resonance occurs at photon energies corresponding to the Cu 3p → 3d but not the 3p → 4s absorption edge.

Analogous resonance photoemission data for $(CH_3NH_3)_2CuCl_4$ are shown in Figure 9b. The satellite peak clearly increases in intensity at photon energies corresponding to the 3p absorption edge, although quantitative analysis is difficult since overlap with the counterion emission prevents an accurate estimate of the satellite off-resonance intensity. Alternatively, peaks A, B, and C are better resolved in this material than in $KCuCl_3$, and there are substantial changes in the shape and relative intensity of these bands as the photon energy increases through the Cu 3p → 3d absorption edge. These changes are presented in Figure 10b which gives the intensity profiles of bands A, B, and C as determined by Gaussian resolution of the valence band spectra.[36] Band A decreases in intensity at resonance (74 eV), while band B shows a small increase. From the spectra taken between 72 and 74 eV, band C changes in intensity in a manner similar to that of band A. The satellite intensity profile shows the dominant enhancement with maxima near 74 and 76.5 eV.

Resonance photoemission spectra were obtained for Cs_2CuCl_4; however, the analysis is complicated by overlap of main peaks A and B with Cs 4d features excited by second-order light. The two small peaks at 11.9 and 9.8 eV, which contain contributions from Cs 5p ionizations (see Figure 6b), show strong resonance enhancement at 73.5-eV photon energy demonstrating additional contributions from $CuCl_4^{2-}$ satellites. As shown in the composite spectra of Figure 8, the binding energy of the more intense, higher binding energy satellite for D_{2d} $CuCl_4^{2-}$ is 0.5 eV less than that observed in either of the tetragonal complexes. The energies

(36) Analysis of this resonant photoemission data is complicated by charging effects which become significant for the spectra taken between 74.8 and 78 eV. The increased charging, most likely caused by the onset of 3p photoemission, shifts the peaks to 1 eV deeper binding energy and alters the shape of the spectra. However, in the photon energy range from 72 to 74 eV the binding energies were constant, and thus the spectral changes in the photoemission data should be most accurate.

Scheme IV

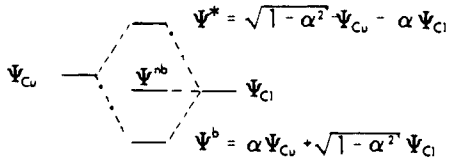

associated with these resonance effects for the D_{4h} $CuCl_4^{2-}$ compounds are summarized in Table IB.

IV. Analysis

A. Ground-State Analysis: Covalent Mixing of Metal 3d and Ligand 3p Orbitals. Several features of the variable energy PES spectra of CuCl and $CuCl_4^{2-}$ are quantitatively different, reflecting differences in metal–ligand bonding between these two materials. In CuCl, the Cu 3d band (A) and the Cl 3p band (B) are separated in binding energy by 4.0 eV. The Cl 3p band decreases in intensity relative to the d band by a factor of 25 as the photon energy increases from 26 to 45 eV. As shown in Figures 2 and 3, very little intensity remains in the Cl 3p band at its Cooper minimum (at 45 eV, $I_A/I_B > 13$).

In D_{4h} $CuCl_4^{2-}$, (Figure 7b) the two main bands, A and B, show a similar relative photon energy dependence as the Cu 3d and Cl 3p bands of CuCl, respectively, and hence have analogous assignments. Bands A and B are separated by only 1.8 eV, however, and while there is still clearly a minimum in intensity of the Cl band B relative to the d band A near 50-eV photon energy, significant intensity still remains in band B at the Cooper minimum (Table II.A), $I_A/I_B = 3.2$ at 48.4 eV. At this photon energy, the Cl 3p contribution to the PES spectrum should be negligible and intensity must arise predominantly from d-orbital ionization, requiring significant Cu 3d character in the Cl 3p band. The decrease in energy separation between the copper 3d and chlorine 3p levels in D_{4h} $CuCl_4^{2-}$ relative to CuCl clearly results in an increase in covalent mixing of the Cu 3d and Cl 3p orbitals of the D_{4h} $CuCl_4^{2-}$ complex. Strong covalent mixing in $CuCl_4^{2-}$ is also required by the absolute photon energy dependence of its d band (Figure 3). For $CuCl_4^{2-}$, band A is more intense than the Cu d band A of CuCl at low photon energies and decreases dramatically with increasing photon energy, indicating significant admixture of Cl 3p cross section.

Covalent bonding in $CuCl_4^{2-}$ also accounts for the appearance of a third band, N, which falls energetically in between bands A and B. Peak N exhibits essentially pure 3p cross section and is assigned as ionization from the ligand nonbonding orbitals. As shown in Scheme IV, simple molecular orbital considerations indicate that photoemission from ligand nonbonding orbitals should lie in the energy region between emission from ligand bonding and metal antibonding molecular orbitals.

In order to analyze quantitatively the observed photoemission intensities in terms of metal–ligand bonding interactions, the photoionization cross sections for the covalently mixed-valence orbitals of D_{4h} $CuCl_4^{2-}$ can be related to atomic cross sections through the Gelius–Siegbahn model.[37] This model assumes that the ionization probability of a molecular orbital (I_{mo}) is equal to the weighted sum of the ionization probabilities from all of its atomic orbital components (σ_{ao}):

$$I_{mo} = \sum_i c_i^2 \sigma_{ao} \qquad (1)$$

where c_i are the molecular orbital mixing coefficients. This expression is most reliable quantitatively when the input photon energy is large (>200 eV) or when the magnitude of one atomic orbital cross section is dominant over all the other atomic orbital contributions to the intensity, justifying the neglect of cross terms between the metal and ligand contributions in eq 1.[38b]

The intensity ratio data at the Cooper minimum and at 1253.6 eV given in Table II.A can be used to obtain an experimental estimate of the covalent mixing (α^2 in Scheme IV) for D_{4h} $CuCl_4^{2-}$ averaged over the initial-state ligand bonding and metal antibonding orbitals. Equation 1 applies at these photon energies and the intensity ratio is related to known atomic photoionization cross sections in the equation:

$$\frac{I_A}{I_B} = \frac{N^*[\alpha^2(\sigma_{3p}) + (1-\alpha^2)(\sigma_{3d})] + (N^{nb}/2)\sigma_{3p}}{N^b[\alpha^2(\sigma_{3d}) + (1-\alpha^2)(\sigma_{3p})] + (N^{nb}/2)\sigma_{3p}} \qquad (2)$$

where from Scheme I, $N^* = 9$ metal antibonding electrons, $N^b = 10$ ligand bonding electrons, and $N^{nb} = 14$ ligand nonbonding electrons that are treated as equally contributing to bands A and B.[34] Fixing the atomic 3d cross section (σ_{3d}) at 0.1, the relative magnitude of the calculated Cl 3p cross section is largest at 22 eV ($\sigma_{3p} = 0.20$), has a value of approximately 0.035 at 1253.6 eV, and is smallest at the Cooper minimum.[8] Two different values of σ_{3p} at 48.4 eV have been considered: a lower estimate of $\sigma_{3p} = 0.00$, and an upper estimate of $\sigma_{3p} = 0.012$ obtained from calculations[8] which also corresponds to the value obtained from the CuCl photoemission intensities at 45 eV (Figure 3) assuming no mixing. For 1253.6 eV, $I_A/I_B = 1.3$ gives a mixing coefficient $\alpha^2 = 0.26$ while at 48.4 eV, $I_A/I_B = 3.2$ gives either $\alpha^2 = 0.22$ (for $\sigma_{3p} = 0.00$) or $\alpha^2 = 0.10$ (for $\sigma_{3p} = 0.012$). The value of $\sigma_{3p} = 0.012$ at the Cooper minimum is an overestimate as part of the intensity of band B in Figure 2 at 45 eV must result from mixing with the 3d orbitals. This initial state model yields an experimental estimate of 75–85% d character in the antibonding wave functions averaged over the d band.

The results of the above simple treatment can be compared to coefficients obtained from self-consistent-field Xα-scattered wave calculations on the ground state of D_{4h} $CuCl_4^{2-}$. It has been found that ground-state SCF–Xα–SW calculations performed with atomic sphere radii determined through the Norman criteria[39] do not give an accurate orbital ordering[40] and overestimate the covalent mixing of ligand and metal orbitals in the ground state.[41] To overcome these problems, the sphere radii in the D_{4h} $CuCl_4^{2-}$ calculations were empirically adjusted to reproduce experimental EPR g values while maintaining matching potentials at the sphere boundaries.[3] This method has been found to give results in good agreement with experimental d–d and charge-transfer transition energies and intensities.[28]

The ground-state orbital energies and charge distributions obtained from Xα calculations for D_{4h} $CuCl_4^{2-}$ are given in Table III.A.[3] The highest energy, half-occupied $d_{x^2-y^2}$ orbital ($3b_{1g}$) is determined to have 61% Cu 3d and 34% Cl 3p character (the remaining 5% being distributed among the inter- and outer-sphere regions). Therefore, in the ground state the unpaired electron is highly delocalized over both the Cu and Cl centers. In order to calculate valence band PES intensities from the Xα charge decomposition, the inter- and outer-sphere charges were repartitioned among the Cu and Cl spheres.[42] The resulting wave functions were renormalized to include only Cu 3d and Cl 3p character[43] and orthogonalized to the lowest binding energy, metal-centered orbital using the Gram–Schmidt technique. The electron weighted average d character contained in the metal antibonding levels is found to be 82% which is in reasonable agreement with the value obtained from the experimental PES intensity data with eq 2.

The Xα–SW calculated energies and wave functions for the ground state of D_{4h} $CuCl_4^{2-}$ were used in combination with the Gelius–Siegbahn model (eq 1) to obtain a theoretical fit to the valence band PES spectrum. This is given in Figure 11b assuming

(37) (a) Gelius, U.; Siegbahn, K. *Faraday Discuss. Chem. Soc.* **1972**, *54*, 257. (b) Gelius, U. *Electron Spectroscopy*; edited by Shirley, D. A., Ed.; North Holland: Amsterdam, 1972.

(38) (a) Ley, L.; Pollak, R. A.; McFeeley, F. R.; Kowalczyk, S. P.; Shirley, D. A. *Phys. Rev. B* **1974**, *9*, 600. (b) Kono, S.; Kobayasi, T. *Solid State Commun.* **1974**, *15*, 1421.

(39) Norman, J. G., Jr. *Mol. Phys.* **1976**, *31*, 1191.

(40) Correa de Mello, P.; Hehenberger, M.; Larsson, S.; Zerner, M. *J. Am. Chem. Soc.* **1980**, *102*, 1278.

(41) (a) Sontum, S. F.; Case, D. A. *J. Phys. Chem.* **1982**, *86*, 1596. (b) Cook, M. R. Ph.D. Thesis, Harvard University, 1981. (c) Sunil, K. K.; Rodgers, M. *Inorg. Chem.* **1981**, *20*, 3283.

(42) Case, D. A.; Karplus, M. *Chem. Phys. Lett.* **1976**, *39*, 33.

(43) Only the $2a_{1g}$ orbital contains significant 4s character.

Table III

A. D_{4h} $CuCl_4^{2-}$ Energy Levels from Xα Calculation

level	energy (eV)	% Cu	% Cl	inter sphere	outer sphere	Cu angular contribution	renormalized + orthogonalized % Cu	renormalized + orthogonalized % Cl
$3b_{1g}$	−2.85	61	34	1	4	99% d	66	34[a]
$2b_{2g}$	−4.31	79	15	4	1	100% d	84	16[a]
$2e_g$	−4.35	74	21	4	1	100% d	78	22[a]
$3a_{1g}$	−4.61	93	2	4	0	5% s, 95% d	98	2[a]
$1a_{2g}$	−4.72	1	87	9	2		0	100[b]
$4e_u$	−5.32	5	83	9	4		0	100[b]
$1b_{2u}$	−5.33	2	83	13	2		0	100[b]
$1e_g$	−6.01	27	60	12	2	98% d	22	78[c]
$2a_{2u}$	−6.06	5	74	19	2		0	100[b]
$1b_{2g}$	−6.77	22	63	14	2	99% d	16	84[c]
$3e_u$	−6.82	19	77	0	4	84% p, 11% f	0	100[b]
$2b_{1g}$	−7.16	46	51	0	3	98% d	34	66[c]
$2a_{1g}$	−8.00	32	65	0	3	67% s, 28% d	2	98[c]
$1b_{1g}$	−17.33	8	92	0	1			
$2e_u$	−17.57	8	91	0	1		Cl 3s	
$1a_{1g}$	−17.96	11	88	0	1	65% s, 21% d		

B. Xα-SW PES Calculated Intensities for D_{4h} $CuCl_4^{2-}$

level	22 eV	Cooper minimum σ_L = 0.012	Cooper minimum σ_L = 0.00	1253.6 eV
$3b_{1g}$	0.134	0.070	0.066	0.078
$2b_{2g}$	0.232	0.172	0.168	0.179
$2e_g$	0.488	0.321	0.312	0.343
$3a_{1g}$	0.204	0.196	0.192	0.197
$1a_{2g}$	0.400	0.024	0.000	0.070
$4e_u$	0.800	0.048	0.000	0.140
$1b_{2u}$	0.400	0.024	0.000	0.070
$1e_g$	0.712	0.125	0.088	0.197
$2a_{2u}$	0.400	0.024	0.000	0.070
$1b_{2g}$	0.368	0.050	0.032	0.091
$3e_u$	0.800	0.048	0.000	0.140
$2b_{1g}$	0.332	0.084	0.068	0.114
$2a_{1g}$	0.396	0.028	0.004	0.073
peak A	1.058	0.759	0.738	0.797
peak B	1.808	0.287	0.192	0.475
peak N	2.80	0.168	0.000	0.490

[a] Antibonding (A). [b] Nonbonding (N). [c] Bonding (B).

σ_{3p} = 0.00 at the Cooper minimum (intensities for individual ionizations are given as a function of photon energy in Table III.B). Also included in Figure 11 are the experimental spectrum (Figure 11d) and the spectrum obtained using a ligand field model, which allows for energy splittings of the d levels due to repulsive interactions with the ligands but no covalent mixing (Figure 11a). The intensities in Figure 11a simply reflect the electron weighted degeneracy of the metal antibonding levels of D_{4h} $CuCl_4^{2-}$. In agreement with the above analysis the covalent mixing redistributes intensity from band A into band B as observed experimentally at the Cooper minimum. The intensity weighted average energy splitting between the metal antibonding and ligand bonding PES peaks is calculated to be 2.0 eV which is in reasonable agreement with the experimental value of 1.8 eV. Summing together contributions from the metal antibonding, ligand bonding, and ligand nonbonding levels, the composite band A to band B intensity ratio calculated as a function of photon energy is given and compared with the data in Table II.B.2. The ratios calculated at the Cooper minimum and 1253.6 eV agree quite well with the experimental values.

B. Relaxation Effects. Despite the generally good agreement mentioned above, there are several problems with this ground-state analysis of the PES spectrum. First, in contrast to CuCl (Figure 4), $CuCl_4^{2-}$ clearly exhibits significant satellite intensity at nonresonance photon energies (Figure 6c). Within the initial state, frozen orbital approximation, however, the satellite corresponds to a two-electron transition which should have no intensity out of resonance. A second complication concerns the nature of the resonance enhancement in that the dominant enhancement for $CuCl_4^{2-}$ occurs in the satellite peaks, while only limited resonance effects occur in the d band (A).

Scheme V

$$\text{Resonance:}\quad 3p^63d^{10} \xrightarrow{\text{Abs}} 3p^53d^{10}4s^1 \xrightarrow{\text{SCK Auger}} 3p^63d^84s^1$$

$$\text{Main PES:}\quad 3p^63d^{10} \longrightarrow 3p^63d^9$$

$$\text{Shake-up PES:}\quad 3p^63d^{10} \longrightarrow 3p^63d^84s^1$$

Scheme VI

$$\text{Resonance}\quad 3p^63d^9 \xrightarrow{\text{Abs}} 3p^53d^{10} \xrightarrow{\text{SCK}} 3p^63d^8$$

Insight into the final states associated with the satellite peaks can be obtained through a comparison of the CIS and CFS spectra of CuCl and $CuCl_4^{2-}$. From Figure 4, CuCl exhibits a satellite peak at 12 eV above the d band which shows the dominant resonance enhancement as the photon energy is scanned through the 3p → 4s absorption edge at 78 eV. The SCK Auger decay mechanism (Scheme V) dictates that this transition will produce resonance enhancement of the $3p^63d^84s^1$ final states, leading to the assignment of the satellite peak in CuCl as a 3d → 4s shake-up transition.[30]

The satellite peaks in $CuCl_4^{2-}$ appear at 8 eV above the metal antibonding band A. Based on the increased effective nuclear charge on Cu(II), the 3p → 4s transition should be higher in energy than for CuCl (Xα calculations predict the 3p → 4s transition to be 4.8 eV higher for $CuCl_4^{2-}$).[35] Thus the CFS peaks at ~81 eV in Figure 10a should be assigned as the 3p → 4s transition requiring that the peak at 73.5 eV be the 3p → 3d transition. As resonance in $CuCl_4^{2-}$ is observed exclusively at the 3p → 3d edge, the SCK Auger decay mechanism requires (Scheme

Table IV. Final-State Energies (eV) for D_{4h} $CuCl_4^{2-}$ from Xα Calculation

	main ionizations			satellite ionizations			
	spin restricted	spin unrestricted triplet	spin unrestricted singlet	spin restricted	spin unrestricted triplet	spin unrestricted singlet	
$3b_{1g}$	5.96						
$2b_{2g}$	7.63	7.45	8.01	11.96			metal antibonding ionization plus shake-up
$2e_g$	7.38	7.22	7.74	11.68			
$3a_{1g}$	8.71	8.45	8.96	13.52			
$1a_{2g}$	7.18			12.00			ligand nonbonding ionization plus shake-up
$4e_u$	7.76			12.56			
$1b_{2u}$	7.75			12.56			
$1e_g$	9.15	8.64	9.86	15.44	14.54	16.94	ligand bonding ionization plus shake-up
$2a_{2u}$	8.41			13.19			
$1b_{2g}$	9.29	9.12	9.86	15.49	14.54	16.96	
$3e_u$	9.38			14.09			
$2b_{1g}$	10.12	9.90	10.71	15.53	15.53		
$2a_{1g}$	10.65	10.50	10.88	15.05	15.05	15.63	
$1b_{1g}$	19.96						

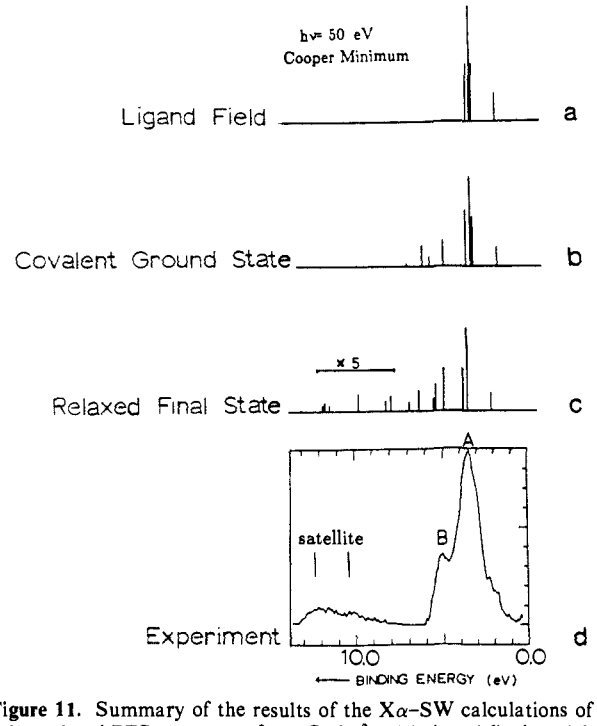

Figure 11. Summary of the results of the Xα–SW calculations of the valence band PES spectrum of D_{4h} $CuCl_4^{2-}$: (a) ligand field model; (b) covalent ground-state analysis; (c) relaxed final-state analysis; and (d) the composite spectrum of $(CH_3NH_3)_2CuCl_4$ (A, B, and C) and $KCuCl_3$ (satellite) at the Cooper minimum.

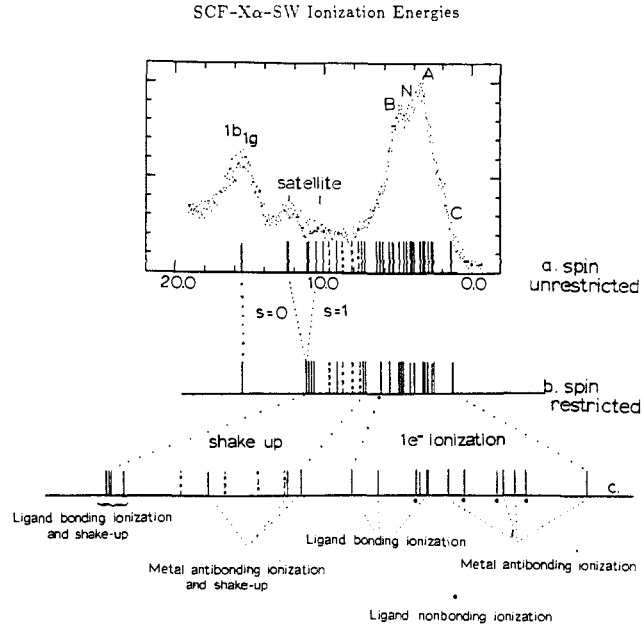

Figure 12. Comparison of calculated SCF–Xα–SW main and satellite energies for D_{4h} $CuCl_4^{2-}$ with experimental $(CH_3NH_3)_2CuCl_4$ valence band XPS data: (a) complete ionization spectrum including multiplet splitting of main and satellite ionizations from a spin-unrestricted calculation; (b) ionization energies without multiplet splitting from a spin-restricted calculation; (c) expanded scale of (b) assigning the calculated peaks. Dashed lines indicate ligand nonbonding ionizations plus shake-up final states which have no intensity.

VI) that resonance enhancement, and therefore the satellite peak, must be associated with the $3d^8$ final state. However, from the initial-state wave functions given in Table III, peak A derives from ionization from metal antibonding orbitals with dominantly d character in the ground state. The resulting frozen orbital final state would correspond to two holes on the metal or a d^8 final-state configuration and lead to a strong resonance enhancement of peak A, which is not observed. Both the resonant enhancement of the satellite peak and its significant intensity out of resonance require large orbital relaxations in the final states.

Relaxation effects in the PES spectra were analyzed using the SCF–Xα–SW formalism. For the one-electron transitions associated with the main peaks (A and B), the ionization energies were calculated using the Slater transition state method (i.e., removal of 0.5 electron from a given orbital and reconverging the potential), while the final-state wave functions were obtained by removing 1.0 electron from the orbital and reconverging the potential.[44] The satellite structure involves ionization with simultaneous shake-up of a second valence electron (of the same symmetry as the ground state (b_{1g}) hole) resulting in a higher energy final state. The energies of all the possible valence shake-up states corresponding to one-electron ionization and Cl 3p ($2b_{1g}$) → Cu 3d ($3b_{1g}$) electron transitions were also calculated using the SCF–Xα–SW method. In these calculations, one valence electron is removed and then the transition state formalism is applied whereby 0.5 electron is transferred from the $2b_{1g}$ to the $3b_{1g}$ orbital. The energy difference between these two partially occupied levels is added to the ionization energy of the main line to give the satellite binding energy. Multiplet splitting of the main and satellite peaks associated with the additional unpaired valence electron in the final state was included through spin-unrestricted transition state calculations of the triplet and $m_s = 0$ determinantal energies [$E_s = 2E_{m_s=0} - E_T$]. The energies, wave functions, and PES intensities of the relaxed final-state Xα–SW calculations on D_{4h} $CuCl_4^{2-}$ are described below.

(i) Energies. The Xα–SW spin-restricted and spin-unrestricted ionization energies for the main and satellite peaks of D_{4h} $CuCl_4^{2-}$ are given in Table IV and are compared to the valence band PES spectrum of $(CH_3NH_3)_2CuCl_4$ in Figure 12 to determine final-

(44) (a) Stater, J. C. *Quantum Theory of Molecules and Solids*; McGraw-Hill: New York, 1974; Vol. 4. (b) Stater, J. C. *Adv. Quantum Chem.* **1972**, *6*, 1.

Table V. D_{4h} Final-State Xα Calculated Wave Functions

ionization						repartitioned & renormalized	
main	final state	% Cu	% Cl	inter sphere	outer sphere	% Cu	% Cl
$3b_{1g}$	$3b_{1g}$	45	51	0	4	47	53
	$2b_{1g}$	61	38	0	1	53	47
$2b_{2g}$	$2b_{2g}$	40	48	10	1	46	54
	$1b_{2g}$	62	32	6	0	54	46
	$3b_{1g}$	46	50	0	4	48	52
	$2b_{1g}$	60	39	0	1	52	48
$2e_g$	$2e_g$	31	58	9	1	35	65
	$1e_g$	70	25	5	0	65	35
	$3b_{1g}$	50	46	0	3	52	48
	$2b_{1g}$	56	42	0	1	48	52
$3a_{1g}$	$3a_{1g}$	76	22	1	1	77	23
	$2a_{1g}$	51	48	0	2	23	77
	$3b_{1g}$	37	60	0	4	38	62
	$2b_{1g}$	69	30	0	1	62	38
$1a_{2g}$	$1a_{2g}$	1	89	9	2	1	99
	$3b_{1g}$	63	34	0	3	65	35
	$2b_{1g}$	45	53	0	3	35	65
$1b_{2u}$	$1b_{2u}$	2	85	11	2	2	98
	$3b_{1g}$	62	34	0	3	65	35
	$2b_{1g}$	45	53	0	2	35	65
$4e_u$	$4e_u$	4	85	8	2	5	95
	$3e_u$	20	77	0	3	95	5
	$3b_{1g}$	62	35	0	3	64	36
	$2b_{1g}$	45	53	0	2	36	64
$1e_g$	$1e_g$	97	2	1	0	94	6
	$2e_g$	5	80	13	2	6	94
	$2b_{1g}$	29	67	0	4	30	70
	$2b_{1g}$	78	21	0	1	70	30
$2a_{2u}$	$2a_{2u}$	5	77	16	2	6	94
	$3b_{1g}$	62	35	0	3	64	36
	$2b_{1g}$	46	52	0	2	36	64
$1b_{2g}$	$1b_{2g}$	93	6	1	0	88	12
	$2b_{2g}$	10	73	15	2	12	88
	$3b_{1g}$	30	66	0	4	31	69
	$2b_{1g}$	77	22	0	1	69	31
$2b_{1g}$	$2b_{1g}$	66	33	0	1	42	58
	$3b_{1g}$	40	56	0	4	58	42
$3e_u$	$3e_u$	21	76	0	3	95	5
	$4e_u$	4	85	9	2	5	95
	$3b_{1g}$	60	37	0	3	62	38
	$2b_{1g}$	47	51	0	2	38	62
$2a_{1g}$	$2a_{1g}$	34	64	0	2	4	96
	$3a_{1g}$	93	4	3	0	96	4
	$3b_{1g}$	57	40	0	3	58	42
	$2b_{1g}$	50	48	0	2	42	58

state assignments. The calculation has been aligned with the data at the Cl 3s ($1b_{1g}$) ionization energy. The agreement between experimental energies and the spin-unrestricted multiplet splitting calculations is quite good and better than with the spin-restricted calculation (Figure 12, a and b). The most significant difference between the calculations is in the satellite region, where the spin-unrestricted highest energy singlet satellite peaks are predicted to be 1.5 eV to deeper binding energy relative to the spin-restricted calculations.

From the expanded spectrum in Figure 12c, ionization from metal antibonding orbitals falls in the region of peak A, while the ligand bonding ionizations fall in the region of peak B, consistent with the ground-state analysis in section IV.A. Both spin-restricted and spin-unrestricted calculations predict a peak at 1.5 eV lower energy than all other one-electron ionizations and in an energy region corresponding to peak C. Thus, peak C can be assigned as the final state resulting from ionization of the lowest energy, half-occupied $3b_{1g}$ orbital. The ligand nonbonding interactions are calculated to fall in between the metal antibonding and ligand bonding ionizations consistent with the assignment of band N in this region.

The Xα–SW calculations predict the ligand bonding ionization plus ligand $2b_{1g} \rightarrow$ metal $3b_{1g}$ shake-up states to lie at deepest energy in the valence band spectrum, in the energy region of the most intense satellite peak (Figure 12). Metal antibonding ionization plus shake-up peaks are calculated to lie to lower energies, in a region of lower PES intensity. The shake-up states from ligand nonbonding ionizations are also calculated to fall in this lower energy region, but can have no intensity (vide infra). Thus, the relatively intense satellite peak at 12.5 eV can now be associated with ligand bonding ionization plus ligand to metal shake-up transitions.

Table VI. Charge Rearrangement (ΔQ) Upon Valence Ionization of D_{4h} $CuCl_4^{2-}$

	ΔQ	
	Cu	Cl
$3b_{1g}$	+0.15	−0.13
$2b_{2g}$	+0.46	−0.35
$2e_g$	+0.90	−0.73
$3a_{1g}$	+0.30	−0.25
$1e_g$	−1.22	+1.05
$1b_{2g}$	−0.54	+0.45
$2b_{1g}$	−0.11	+0.11
$2a_{1g}$	0.00	0.00

(ii) Wave Functions. The presence of both significant satellite intensity out of resonance and dominant resonance enhancement of the satellite rather than peak A require large changes in the final-state wave functions on ionization. The Xα–SW determined mixing coefficients of the final-state wave functions resulting from one-electron ionization are presented in Table V, where only the coefficients of orbitals with the same symmetry as the partially occupied final-state levels are given.[45] Comparison of the relaxed final-state coefficients with those of the initial state (Table III) shows substantial change in the levels involved in strong bonding interactions (those of b_{1g}, e_g, a_{1g}, and b_{2g} symmetry). In all cases, the metal antibonding levels of the initial state become more ligand in character upon ionization while the ligand bonding levels acquire dominantly metal character in the relaxed final state. The ligand nonbonding wave functions of b_{2u}, a_{2u}, a_{2g}, and e_u symmetry, however, remain unchanged relative to the initial state.

Changes in the wave functions upon ionization are due to the rearrangement of electron density in response to creation of a valence hole. This rearrangement may be quantified (eq 3) by

$$\Delta Q_i = \sum_{j \neq i} (Q_{j,\mathrm{FS}} - Q_{j,\mathrm{GS}}) \qquad (3)$$

comparing the difference in the total charge density (ΔQ) in the Cu and Cl spheres of the passive orbitals j before ($Q_{j,\mathrm{GS}}$) and after ($Q_{j,\mathrm{FS}}$) ionization from level i (Table VI).[46] For example, ionization of a $2e_g$ electron would leave a hole in an orbital with predominantly metal d character in the frozen orbital approximation. The energy of this final state, however, is lowered by relaxation of the electron density in the $1e_g$, $3b_{1g}$, and $2b_{1g}$ orbitals, changing the final-state wave functions such that 0.9 of an electron is transferred from the Cl sphere to the Cu sphere to screen the hole. The opposite effect is observed for ionization of the $1e_g$ ligand orbital. The magnitude of this charge rearrangement for the metal and ligand orbitals of b_{1g}, b_{2g}, e_g, and a_{1g} symmetry is listed in Table VI. The wave functions do not change upon ionization from ligand nonbonding levels as the lack of d orbital mixing prevents charge flow from the Cu sphere to the Cl sphere.

Finally, as the strong resonance enhancement of the satellite demonstrates that it corresponds to an ionized final state with mostly d^8 (two-hole metal) character, the d^8 character predicted by the Xα–SW calculations for both the frozen orbital and relaxed final states was determined. The d^8 character is given by the many-electron wave functions in Table VII, parts A and B, which are product functions of the two half-occupied molecular orbitals in Table III (frozen orbital) and Table V (relaxed final states). Note that these wave functions are written in terms of two-hole $|1,2\rangle$ character, where $\underline{d}$ indicates a hole in a metal-centered orbital

(45) While a complete set of final-state orbital coefficients were obtained for each of the possible valence ionizations of the complex, only those levels included in Table V show significant changes relative to the initial state levels on ionization.

(46) Case, D. A.; Cook, M.; Karplus, M. *J. Chem. Phys.* **1980**, *73*, 3294.

Table VII. Two-Hole Final State Xα–SW Wave Functions for D_{4h} $CuCl_4^{2-}$

	$\|\underline{d_1}d_2\rangle$	$\|d_2\underline{L_1}\rangle$	$\|\underline{d_1}L_2\rangle$	$\|\underline{L_1}\underline{L_2}\rangle$
A. Frozen Orbital Approximation with Ground-State Xα Calculations				
Metal Antibonding Ionization				
$3b_{1g}$	0.657	−0.475	−0.475	0.343
$2e_g$	0.717	−0.518	−0.378	0.273
$2b_{2g}$	0.745	−0.539	−0.320	0.231
$3a_{1g}$	0.801	−0.579	−0.125	0.090
Ligand Bonding Ionization				
$2b_{1g}$	0.475	−0.343	0.657	−0.475
$1e_g$	0.378	−0.273	0.717	−0.518
$1b_{2g}$	0.320	−0.231	0.745	−0.539
$2a_{1g}$	0.125	−0.090	0.801	−0.578
Metal Antibonding Ionization plus Shake-up				
$2e_g$	0.519	0.718	−0.273	−0.378
$2b_{2g}$	0.539	0.745	−0.231	−0.321
$3a_{1g}$	0.579	0.801	−0.090	−0.125
Ligand Bonding Ionization Plus Shake-up				
$2b_{1g}$	0.343	0.475	0.475	0.657
$1e_g$	0.273	0.378	0.519	0.718
$1b_{2g}$	0.231	0.320	0.539	0.795
$2a_{1g}$	0.090	0.125	0.579	0.657
B. Relaxed Xα Calculations				
Metal Antibonding Ionization				
$3b_{1g}$	0.471	−0.499	−0.499	0.530
$2e_g$	0.426	−0.404	−0.587	−0.557
$2b_{2g}$	0.468	−0.488	−0.509	0.531
$3a_{1g}$	0.526	−0.677	−0.316	0.407
Ligand Bonding Ionization				
$2b_{1g}$	0.493	−0.583	0.417	−0.493
$1e_g$	0.525	−0.822	0.199	−0.187
$1b_{2g}$	0.515	−0.787	0.187	−0.286
$2a_{1g}$	0.155	−0.129	0.754	−0.626
Metal Antibonding Ionization Plus Shake-up				
$2e_g$	0.404	0.426	−0.557	−0.587
$2b_{2g}$	0.488	0.468	−0.531	−0.316
$3a_{1g}$	0.677	0.526	−0.407	−0.316
Ligand Bonding Ionization Plus Shake-up				
$2b_{1g}$	0.583	0.493	0.493	0.417
$1e_g$	0.822	0.525	0.187	0.119
$1b_{2g}$	0.787	0.515	0.286	0.187
$2a_{1g}$	0.129	0.155	0.626	0.754

and $\underline{L}$ indicates a hole in a ligand-centered orbital. The frozen orbital calculations (Table VII.A) predict that the metal antibonding ionizations, band A, have the highest two-hole metal $|\underline{d_1}d_2\rangle$ character, 53%, which is inconsistent with experiment (i.e., no significant resonance enhancement is observed for peak A). Inclusion of final-state relaxation (Table VII.B) greatly decreases the amount of $|\underline{d_1}d_2\rangle$ character in the metal antibonding ionized states (to 22%) and distributes the d^8 character into the shake-up final states, with 47% in the ligand ionization plus shake-up and 26% in the metal ionization plus shake-up. The amount of d^8 character in the ligand ionization plus shake-up states is expected to increase with increased correlation (see CI analysis, section IV.C). The observed dominant resonance enhancement of the satellite peaks associated with ligand ionization plus shake-up is, therefore, in agreement with the relaxed Xα final-state wave functions.

(iii) Intensities. The changes in wave function on ionization also result in the presence of satellite intensity out of resonance. The greater the change in wave function, the greater will be the satellite intensity produced. The frozen orbital final states can be expanded in terms of the relaxed final states of the ion using the sudden approximation:[7]

$$\psi_R(N-1) = \sum_{i=0}^{\infty} \langle \psi_i | \psi_R \rangle \psi_i(N-1) \qquad (4)$$

Table VIII. Intensity Redistribution as Calculated by the Sudden Approximation[a]

	Main Ionization	Redistributed Intensity			
metal antibonding ionization	$3b_{1g}$	0.931 (a)	6.8×10^{-2} (b)	1.2×10^{-3} (c)	
	$2b_{2g}$	0.806 (d)	0.162 (e)	2.7×10^{-2} (f)	5.5×10^{-3} (g)
	$2e_g$	0.791 (d)	0.193 (e)	1.4×10^{-2} (f)	3.4×10^{-3} (g)
	$3a_{1g}$	0.792 (d)	0.131 (e)	6.8×10^{-2} (f)	1.1×10^{-2} (g)
ligand bonding ionization	$1e_g$	0.499 (d)	0.365 (e)	7.8×10^{-2} (f)	5.8×10^{-2} (g)
	$1b_{2g}$	0.465 (d)	0.410 (e)	6.7×10^{-2} (f)	6.0×10^{-2} (g)
	$2b_{1g}$	5.5×10^{-2} (a)	0.890 (b)	5.5×10^{-2} (c)	
	$2a_{1g}$	2.3×10^{-3} (d)	0.992 (e)	8.4×10^{-6} (f)	4.5×10^{-3} (g)

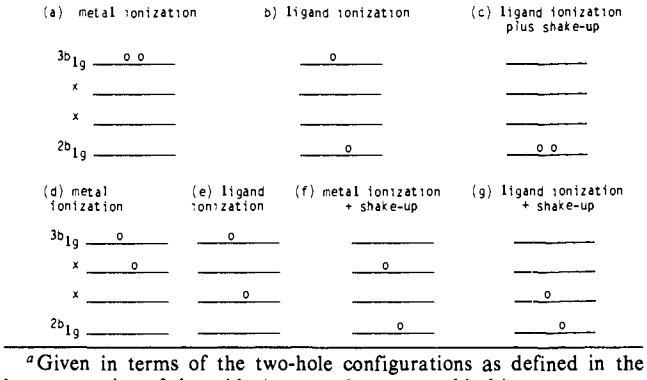

[a] Given in terms of the two-hole configurations as defined in the bottom portion of the table (x = a_{1g}, b_{2g}, or e_g orbitals)

where $\psi_R(N-1)$ is the remainder wave function of the frozen orbital state after one-electron ionization, and $\psi_i(N-1)$ are the ground and excited states of the relaxed ion. These relaxed final states must have the same symmetry as the frozen orbital states, and their relative photoionization intensities are given by the squares of the overlap integrals in eq 4. The total intensity to the $\psi_R(N-1)$ frozen orbital state therefore becomes partitioned among all of the possible final states of the relaxed ion.

The complete intensity calculation for D_{4h} $CuCl_4^{2-}$ involves taking the frozen orbital intensity obtained from using the initial-state wave functions with the Gelius–Siegbahn expression (Table III.B) and redistributing this intensity among relaxed final states of the same symmetry using the orthonormal ψ_R in Table III.A and ψ_i in Table V in eq 4.[47] The intensity distribution for ionizing the metal and ligand orbitals of b_{1g}, e_g, a_{1g}, and b_{2g} symmetry are given in Table VIII. As the ψ's of the ligand nonbonding orbitals do not change upon ionization, the intensity of these features is simply obtained from the frozen orbital approximation. For most of the metal antibonding and ligand bonding ionizations, the majority of the intensity remains in the main peak while 10–20% becomes redistributed among the other main band and the satellites. For two of the ligand bonding ionizations, $1e_g$ and $1b_{2g}$, about half of the intensity actually becomes redistributed into peak A, indicating that the main valence band peak intensity ratio A/B can also change due to relaxation.

The results of the sudden approximation calculation for the A/B and satellite/main peak PES intensity ratios for several different photon energies are given in Table II.B.3. In Figure 11, the energy and Cooper minimum intensity predicted by the relaxed final-state calculation are compared with the results of the ligand-field calculation (a), the ground-state calculation (b), and the data (d). The ligand-field calculation (Figure 11a) places all intensity (which derives only from d character at this photon energy) in band A. As indicated in section IV.A, covalent mixing in the ground state distributes intensity into peak B, and the intensity ratio calculation for the two lowest energy main peaks is comparable to that ob-

(47) The intensity calculation of Loubriel, G. *Phys. Rev. B* **1979**, *20*, 5339, was not used as it requires tangential spheres and rigorously orthonormal final-state wave functions.

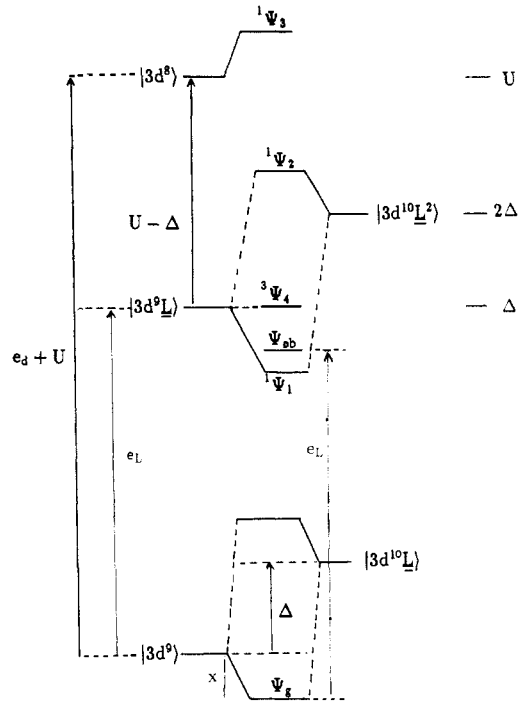

Figure 13. Initial and final-state energies in the Configuration Interaction (CI) model of d^9 photoemission (see text for details).

served experimentally for $CuCl_4^{2-}$ (Table II). The results of the relaxed final-state calculation show small yet important differences from the covalent initial-state analysis. The majority of the intensity is still contained in the low binding energy peaks which correspond to metal antibonding and ligand bonding ionizations in the initial-state model. However, the predicted intensity ratio of these features has been modified (for example, at the Cooper minimum the intensity of band A has decreased relative to band B). Of particular importance, the shake-up final states acquire nonnegligible PES intensity in the relaxed final state which was forbidden in the frozen orbital approximation. The satellites are calculated to have 5% of the nonresonance intensity of the main bands, while experimentally they have 9% at 50 eV. Also, the calculated intensity is fairly equally distributed among the shake-up states associated with both ligand and metal ionizations (Figure 11c) while experimentally the dominant satellite intensity appears in the ligand ionization plus shake-up states to deeper binding energy. These differences between calculated and observed satellite intensity likely relate to the limitation of the Xα method in using only a single determinant to describe the wave function.[48] More correlation is included in the Configuration Interaction analysis of the PES data below, producing increased d^8 character in the relaxed ligand ionization plus shake-up states.

C. Configuration Interaction Model. A Configuration Interaction (CI) model has been developed by Sawatzky,[6b] Davis,[11] and van der Laan[6c] to interpret the nonresonance and resonance intensity of valence band satellite peaks. This model extends the simple treatment given in Scheme IV and eq 2 to include approximately the effects of final-state relaxation and electron correlation. In this section we present a version of this model and apply it to fit the energy splittings in the PES spectrum of D_{4h} $CuCl_4^{2-}$ to obtain an additional experimental estimate of covalent mixing and qualitative insight into the relaxation mechanism. The results of this simple model are then compared with those obtained from the relaxed Xα–SW calculation given in the previous section. Finally, this CI model is used to obtain some quantitative insight into the resonance intensity profile of the satellite peak.

(i) CI Model. As diagrammed at the bottom of Figure 13, the ground-state energy stabilization, x, and wave function, ψ_g, of a

Scheme VII

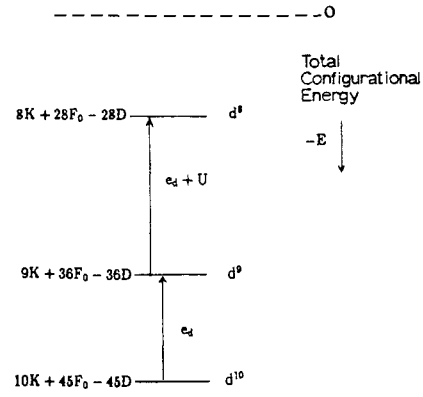

d^9 metal ion complex are obtained by diagonalizing the energy matrix (eq 5), where $|3d^9\rangle$ and $|3d^{10}\underline{L}\rangle$ represent the one-hole

$$\begin{vmatrix} |3d^9\rangle & |3d^{10}\underline{L}\rangle \\ -E & T_1 \\ T_1 & \Delta_1 - E \end{vmatrix} = 0 \qquad (5)$$

metal and d^{10} metal, one-hole ligand configurations respectively. In eq 5, $\Delta_1 = \langle 3d^{10}\underline{L}|H|3d^{10}\underline{L}\rangle - \langle 3d^9|H|3d^9\rangle$, the difference in energy between the two configurations before interaction which is equal to $e_L - e_d$ where e_d (e_L) is the ionization energy of a metal d (ligand) electron, and $T_1 = \langle 3d^{10}\underline{L}|H|3d^9\rangle$, the configuration interaction matrix element. Diagonalization gives:

$$x = \sqrt{\Delta_1^2 + 4T_1^2}/2 - \Delta_1/2$$
$$\psi_g = \cos\theta|3d^9\rangle - \sin\theta|3d^{10}\underline{L}\rangle \qquad (6)$$

where $\tan 2\theta = 2T_1/\Delta_1$. In the simple case of a one-hole complex, the coefficients $\cos\theta$ and $\sin\theta$ should be equivalent to the coefficients determined in the calculations of section IV.A for the $^2B_{1g}$ ground state.

We first consider the effects of ionization of a b_{1g} electron which produces final states with a second hole in a b_{1g} level. This generates three possible configurations $|d^8\rangle$, $|d^9\underline{L}\rangle$, and $|d^{10}\underline{L}^2\rangle$ initially at energies 0, Δ_1, and $2\Delta_1$ above the $3d^8$ configuration energy. However, to these diagonal energies one must include relaxation effects which result from changes in electron repulsion which occur on ionizing the $|d^9\rangle$ and $|d^{10}\underline{L}\rangle$ configurations. Working within the reasonable approximation that changes in metal-centered electron–electron repulsion dominate relaxation, the total energy of the d^{10}, d^9, and d^8 configurations are given in Scheme VII, the d^{10} being most stable.[49] (In Scheme VII, $D = -(14/9)F_2 - 14F_4$.) The expressions in Scheme VII contain terms due to the one-electron integrals (K) which include the kinetic and potential energy of the electron in the field of the nucleus (negative numbers), and the two-electron repulsion Slater integrals (F_0, F_2, F_4, positive numbers). The values of these integrals depend specifically on the radial wave function of the metal ion, and can therefore be sensitive to oxidation state. The binding energy of an electron in the d^{10} metal ion is equal to the difference in the total energy of the d^{10} and d^9 configurations;[49,50] therefore, the ionization energy is equal to:

$$E(d^9) - E(d^{10}) = -K - 9F_0 + 9D = e_d \qquad (7a)$$

a positive number. Similarly, the ionization energy of d^9 is equal to:

$$E(d^8) - E(d^9) = -K - 8F_0 + 8D = e_d + U \qquad (7b)$$

where $U = F_0 - D$ and is also a positive number. Thus, the ionization energy of the d^{10} ion is less than the ionization energy of the d^9 ion by an amount U, the Coulomb repulsion integral.[51]

(48) Connolly, J. W. D. *Semiempirical Methods of Electronic Structure Calculation*, Part A: Techniques; Segal, G. A., Ed., Plenum Press: New York, 1977.

(49) Ferguson, J. *Prog. Inorg. Chem.* **1970**, *12*, 159.

(50) (a) Cardona, M.; Ley, L. *Photoemission in Solids I*; Cardona, M., Ley, L., Eds.; Springer Verlag: Berlin, 1978. (b) Griffith, J. S. *The Theory of Transition Metal Ions*; Cambridge University Press: London, 1961.

(51) Anderson, P. W. *Phys. Rev.* **1959**, *115*, 2.

Scheme VIII

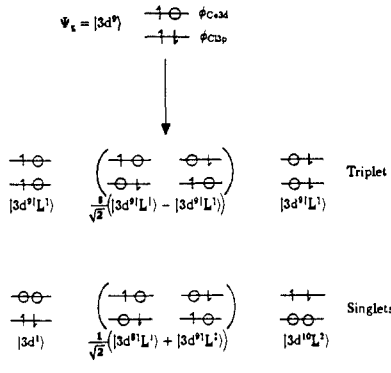

Inclusion of the $|d^9\rangle$ ionization energy in Figure 13 puts the $|d^8\rangle$ final state at $e_d + U$ above the $|d^9\rangle$ configurational energy, while ionization of a ligand electron results in the $|3d^9\underline{L}\rangle$ final state at an energy e_L above the $|d^9\rangle$ configuration. The $|3d^8\rangle$ final-state configuration is then at $U - \Delta_1$ above $|3d^9\underline{L}\rangle$. Fixing the $|d^9\underline{L}\rangle$ energy at Δ_1, the final configurational energies obtained are $|d^8\rangle$ at U and $|d^{10}\underline{L}^2\rangle$ at $2\Delta_1$.

As indicated in Scheme VIII, with b_{1g} valence ionization the $|d^8\rangle$ and $|d^{10}\underline{L}^2\rangle$ configurations each produce one singlet state, while the $|d^9\underline{L}\rangle$ produces both a singlet state and a triplet state. The singlets all have the same spin and same symmetry and can undergo Configurational Interaction which is given by the secular determinant in eq 8a producing the final-state singlet wave

$$\begin{array}{c} \begin{matrix} |d^8\rangle & |d^9\underline{L}\rangle & |d^{10}\underline{L}^2\rangle \end{matrix} \\ \begin{vmatrix} U-E & T_1\sqrt{2} & 0 \\ T_1\sqrt{2} & \Delta_1 - E & T_1\sqrt{2} \\ 0 & T_1\sqrt{2} & 2\Delta_1 - E \end{vmatrix} = 0 \end{array} \quad (8a)$$

functions (eq 8b), where n = 1–3. Note that in eq 8a, the in-

$$^1\psi_n = \alpha_n|d^8\rangle + (\beta_n/\sqrt{2})[|d^9\uparrow\underline{L}^\downarrow\rangle + |d^9\downarrow\underline{L}^\uparrow\rangle] + \gamma_n|d^{10}\underline{L}^2\rangle \quad (8b)$$

teraction matrix element T_1 is the same as in the ground state, an approximation which ignores any orbital contraction that occurs on ionization which would reduce the value of T in the final state.[52] No Configuration Interaction can occur for the triplet state $^3\psi_4$, and this state remains at the $|d^9\underline{L}\rangle$ configuration energy, Δ_1. Finally, in Figure 13 we also include the final state associated with ionizing an electron from a ligand nonbonding orbital, ψ_{nb}, as a reference level at energy e_L above that of the CI stabilized ground state.

The intensities of PES peaks can be estimated within the CI model by evaluating the electric dipole operator between the initial and relaxed final states, $I \propto \langle\psi_g|\vec{r}|\psi_n\rangle^2$. Following the analysis of Davis[11] and van der Laan,[6c] the intensities of transitions to the singlet states produced by b_{1g} ionization, I_n with n = 1–3, are equal to:

$$I_n = [\sqrt{\sigma_d}\,(\alpha_n \cos\theta) + (\beta_n/\sqrt{2}) \times (\sqrt{\sigma_L}\cos\theta - \sqrt{\sigma_d}\sin\theta) - \sqrt{\sigma_L}(\gamma_n \sin\theta)]^2 = \sigma_d[\alpha_n\cos\theta - (\beta_n/\sqrt{2})\sin\theta]^2 + \sigma_L[(\beta_n/\sqrt{2})\cos\theta - \gamma_n\sin\theta]^2 \quad (9)$$

where σ_d (σ_L) is the atomic photoionization cross section for Cu 3d (Cl 3p) ionization, and the cross terms between ligand and metal ionizations have not been included. The intensity of the triplet state PES peak is equal to:

$$I_4 = \tfrac{3}{2}(\sigma_d \sin^2\theta) + \tfrac{3}{2}(\sigma_L \cos^2\theta) \quad (10)$$

The total singlet and triplet intensity is proportional to ionization of the three b_{1g} electrons. The intensity of ψ_{nb} is simply equal to σ_L weighted by the 14 electrons contained in the nonbonding ligand orbitals.

To complete the analysis for the D_{4h} $CuCl_4^{2-}$ photoemission spectrum, one needs to include the energy and intensity of ionizations due to the remaining ligand bonding and metal antibonding orbitals of non-b_{1g} symmetry. The Configurational Interactions for the e_g, a_{1g}, and b_{2g} levels are given by Δ_2 and T_2. Ionization of an electron from one of these orbitals produces a configuration with two holes in levels of different symmetries (a hole formalism is used where the indices 1 and 2 refer to the initial b_{1g} and the ionized orbital, respectively). Both a singlet and a triplet final state are produced which are treated as degenerate. The matrix describing the energies and wave functions for each final state of one electron ionization is given in eq 11,[6c] The final-state wave

$$\begin{array}{c} \begin{matrix} |d_1d_2\rangle & |d_1L_2\rangle & |d_2L_1\rangle & |L_1L_2\rangle \end{matrix} \\ \begin{vmatrix} U-E & T_1 & T_2 & 0 \\ T_1 & \Delta_1 - E & 0 & T_2 \\ T_2 & 0 & \Delta_2 - E & T_1 \\ 0 & T_2 & T_1 & \Delta_1 + \Delta_2 - E \end{vmatrix} = 0 \end{array} \quad (11)$$

functions obtained from eq 11 are of the form given in eq 12a,

$$\psi_{n'} = \alpha_{n'}|d_1d_2\rangle + \beta_{n'}|d_1L_2\rangle + \gamma_{n'}|d_2L_1\rangle + \delta_{n'}|L_1L_2\rangle \quad (12a)$$

where n' = 1 to 4. The intensity for each of the four states, $I_{n'}$, is given by eq 12b. The sum of the intensities of the four $I_{n'}$

$$I_{n'} = [(\alpha_{n'}\sqrt{\sigma_d} + \gamma_{n'}\sqrt{\sigma_L})\cos\theta - (\beta_{n'}\sqrt{\sigma_d} + \delta_{n'}\sqrt{\sigma_L})\sin\theta]^2 \quad (12b)$$

ionizations is proportional to the total intensity of ionizing two electrons.[6c] The intensity of $I_{n'}$ must be weighted according to the specific orbital degeneracy giving a total intensity proportional to 16 electrons.

(ii) Application to D_{4h} $CuCl_4^{2-}$. In applying the CI model to D_{4h} $CuCl_4^{2-}$, we first consider the b_{1g} levels. In the limit of no metal–ligand mixing ($T_1 = 0$) and no change in electron–electron repulsion ($U = 0$) the relative energy order is $^1\psi_1$ ($E = 0$), $^1\psi_2{}^3\psi_4$ ($E = \Delta_1$), $^1\psi_3$ ($E = 2\Delta_1$). The ground state is pure $|3d^9\rangle$ and d electron ionization produces intensity only in $^1\psi_1$ (band A) which corresponds to the pure $|3d^8\rangle$ final state. As ground-state mixing increases ($T_1 > 0_1$, $\cos\theta < 1$) some ionization intensity becomes redistributed from $^1\psi_1$ into $^1\psi_2$ and $^3\psi_4$; $^1\psi_1$ and $^1\psi_3$ split symmetrically about $^1\psi_2$, $^3\psi_4$. This situation corresponds to the frozen orbital approximation as discussed in section IV.A where ground-state covalent mixing induces metal ionization intensity into band B ($^1\psi_2$, $^3\psi_4$). If U is now increased to a large value relative to Δ_1, $^1\psi_2$ splits away from $^3\psi_4$ due to CI mixing, and $^1\psi_3$ moves to significantly deeper binding energy (see Figure 13). Here $^1\psi_3$ corresponds to the high binding energy satellite with a wave function containing predominantly $|3d^8\rangle$ character. Experimental values for T_1, Δ_1, and U for the b_{1g} levels were determined by matching the energy positions of the $^1\psi_1$, ψ_{nb}, $^3\psi_4$, and $^1\psi_3$ final states with the experimental PES binding energies of the main bands A, N, B, and the satellite peaks, respectively. $^1\psi_3$ is placed at an energy corresponding to the intensity weighted average of the binding energies of the two satellite peaks. The $^1\psi_1$ and $^3\psi_4$ states were fit so as to straddle the width of the valence band peaks A and B which places $^1\psi_1$ in the energy region of peak C. The ligand nonbonding ionizations fall in the middle of the two main valence band peaks as observed experimentally (band N). This fitting procedure determines that for D_{4h} $CuCl_4^{2-}$, T_1 = 1.95, U = 6.5, and Δ_1 = 1.2 eV, corresponding to a b_{1g} ground-state wave function with $\cos^2\theta$ = 64.7% Cu 3d and $\sin^2\theta$ = 35.3% Cl 3p character, in good agreement with the ground-state SCF–Xα–SW calculation.

To complete the analysis for D_{4h} $CuCl_4^{2-}$, $\Delta_1 = \Delta_2$, but T_1 must be larger than the T_2 values for all the levels of e_g, a_{1g}, and b_{2g} symmetry since $3b_{1g}$ is the lowest binding energy (most antibonding) level. The values of the T_2's were estimated from the ligand field and charge transfer absorption spectra of the tetragonal $(C_2H_5NH_3)_2CuCl_4$ complex.[53] The T_2 values used for the photoemission spectrum ($T_2(a_{1g})$ = 0.79, $T_2(b_{2g})$ = 0.64, $T_2(e_g)$ = 0.53) have been scaled by a factor of 0.79 relative to those de-

(52) (a) Fujimori, A.; Minami, F. *Phys. Rev. B* **1984**, *30*, 957. (b) Fujimori, A.; Minami, F.; Sugano, S. *Ibid.* **1984**, *29*, 5225.

(53) Cohen, S. L. Ph.D. Thesis, Massachusetts Institute of Technology, 1986.

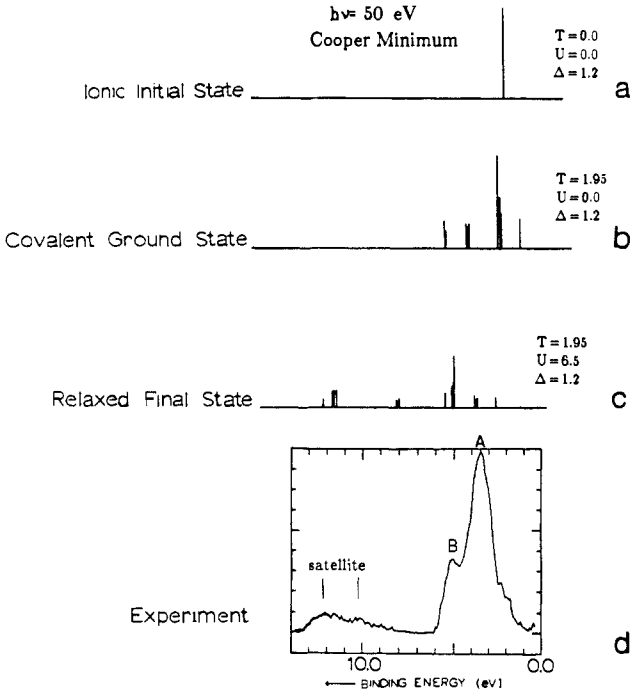

Figure 14. Summary of the results of the Configuration Interaction calculations of the valence band photoemission spectrum of D_{4h} $CuCl_4^{2-}$. The pertinent CI parameters are listed on the figure. Format of figure parallels that in Figure 11.

termined from the optical spectrum so that T_1 from the optical data equals the value obtained above from UPS. Addition of the ionizations from these levels to the states present from the b_{1g} and nonbonding ligand orbital ionizations generates a complete valence band spectrum. The above values of T give an initial-state mixing averaged over the metal antibonding levels of 82% Cu 3d, 18% Cl 3p, which is in excellent agreement with the ground-state Xα results and the experimental Gelius–Siegbahn intensity analysis.

This best fit to the D_{4h} $CuCl_4^{2-}$ valence band spectrum using these parameters and allowing only for contributions from d ionization (i.e., $\sigma_L = 0$) is compared with the $h\nu = 50$ eV spectrum in Figure 14c. Figure 14 should be correlated to the analogous results for the SCF–Xα–SW calculation in Figure 11. The overall energy fit of the CI calculation to the PES spectrum is quite good with a satellite peak predicted at a binding energy of 8.0 eV, analogous to the SCF–Xα–SW transition-state calculation. However, the intensity of the features predicted with this best set of CI parameters is not in even qualitative agreement with the photoemission spectrum. The CI calculated ratio of the main bands (A + 0.5N)/(B + 0.5N) at the Cooper minimum is only 0.32 (Table II.C.2), while experimentally this ratio is 3.2. Even if the Cl 3p cross section is increased to $\sigma_L = 0.012$, which is an upper estimate at this photon energy, the predicted intensity ratio of 0.55 does not approach the experimental value. In addition, the photon energy dependence of the valence band intensities predicted by the CI formalism is not consistent with that observed experimentally as the (A + 0.5N)/(B + 0.5N) ratio actually goes through a minimum near 50 eV (Table II.C.2). Finally, the satellite peak, which is observed experimentally to have 9% of the total main band intensity, is predicted by the CI model to have 55% of the main valence band intensity at 50 eV. Far better agreement with experimental peak intensities is obtained if U is set equal to 0 in the CI model, giving a frozen orbital calculation (covalent initial state in Figure 14b). At this level of calculation, there can be no intensity in the satellite peak, and most of the intensity is present in peak A, giving a reasonable A/B intensity ratio of 3.87 with $\sigma_{3p} = 0.00$ (Table II.C.1).

Thus, while the CI formalism applied to the D_{4h} $CuCl_4^{2-}$ PES spectrum gives good binding energy agreement and a reasonable estimate of the ground-state wave function, the intensities predicted for the relaxed final states are poor. It is important to consider

Table IX. Final-State Wave Function Calculated for D_{4h} $CuCl_4^{2-}$ Using Configuration Interaction Model: $U = 6.5$, $T_1 = 1.95$, $\Delta = 1.2$; $T_2 = 0.79$ (a_{1g}), 0.64 (b_{2g}), 0.53 (e_g)[a]

	$\|d_1\underline{d_2}\rangle$	$\|d_1\underline{L_1}\rangle$	$\|d_1\underline{L_2}\rangle$	$\|\underline{L_1}\underline{L_2}\rangle$
		Band A (Band C)		
$^1\psi_1$ (b_{1g})	0.270	−0.561	−0.561	0.544
ψ_1 (a_{1g})	0.198	−0.450	−0.674	0.552
ψ_1 (b_{2g})	0.178	−0.410	−0.700	0.558
ψ_1 (e_g)	0.160	−0.372	−0.720	0.564
		Band B		
$^3\psi_4$ (b_{1g})	0.000	−0.707	0.707	0.000
ψ_2 (a_{1g})	0.221	−0.833	0.477	−0.175
ψ_2 (b_{2g})	−0.224	0.855	−0.425	0.173
ψ_2 (e_g)	0.260	−0.873	0.380	−0.164
		States at 8 eV		
$^1\psi_2$ (b_{1g})	0.421	−0.291	−0.291	−0.809
ψ_3 (a_{1g})	−0.217	0.083	0.542	0.808
ψ_3 (b_{2g})	0.179	−0.064	0.560	0.807
ψ_3 (e_g)	−0.151	0.052	0.570	0.806
		Satellite		
$^1\psi_3$ (b_{1g})	0.866	0.316	0.316	0.223
ψ_4 (a_{1g})	−0.930	−0.313	−0.157	−0.113
ψ_4 (b_{2g})	−0.937	−0.312	−0.129	−0.094
ψ_4 (e_g)	−0.941	−0.312	−0.109	−0.079

[a] ψ's are defined in text.

the two factors contributing to the spectral intensity in the relaxed final-state calculations: the final-state wave functions and the intensity mechanisms used in the CI and Xα–SW calculations. The CI wave functions which correspond to the best fit given in Figure 14c with $U = 6.5$ eV are listed in Table IX. The satellite wave functions are predominantly composed of $|3d^8\rangle$ character while the states corresponding to peak A are primarily a mixture of 65% $|3d^9\underline{L}\rangle$ and 31% $|3d^{10}\underline{L}^2\rangle$ character. As discussed earlier, it is the significant $|3d^8\rangle$ character in the satellite which is responsible for its dramatic resonance behavior. Comparing Tables IX and VII it is clear that the inclusion of relaxation in the Xα and CI calculations induces the same general changes in the wave functions. In both cases there is an overall loss of $|3d^8\rangle$ character in band A and an increase of $|3d^8\rangle$ component in the satellite. The satellite is more ionic in the CI calculation containing an average of 85% $|3d^8\rangle$ character relative to the Xα calculation value of 47%, which is a consequence of the higher correlation present in the CI model.

In contrast to the small differences in the CI and Xα final-state wave functions in Tables IX and VII.B, the mechanisms used to determine the intensities from these final-state wave functions are different and result in the significant differences in calculated intensity. The sudden approximation used in section IV.B for the Xα analysis assumes that the ionization event occurs rapidly.[7] This allows the formation of satellite states as well as the main ionizations as described by eq 4. The intensity formalism used in the CI analysis uses an adiabatic approximation, where the transition moment from the ground state to the fully relaxed final state is calculated.[11,6c] The adiabatic approximation assumes that the passive electrons adjust to the new potential during ionization. These two different levels of approximation predict very different intensity distributions in the final-state spectrum independent of the final-state wave functions used. To analyze the effect of using the adiabatic approximation on predicted PES intensities, the SCF–Xα–SW wave functions of Table VII.B were used to generate the $CuCl_4^{2-}$ spectral intensities at the Cooper minimum with eq 12b. The A/B intensity ratio calculated this way is 0.78, significantly less than that calculated using the sudden approximation (2.84, from Table II.B.3) and in poor agreement with experiment. The satellite to main peak intensity ratio is 0.33, much larger than given by the sudden approximation. It is the adiabatic approximation, therefore, that is responsible for the poor CI calculated intensity ratios rather than the CI final-state wave functions. Clearly the sudden approximation intensity calculation generates a more consistent fit to the D_{4h} $CuCl_4^{2-}$ data with both CI and Xα–SW wave functions.

Table X. D_{2d} $CuCl_4^{2-}$ Xα Calculated Energy Levels and Wave Functions

level	energy (eV)	% Cu	% Cl	inter sphere	outer sphere	Cu angular contribution	renormalized % orthogonalized % Cu 3d	4p	% Cl
$5b_2$	-2.96	71	25	0	3	4% p, 94% d	71	3	26
6e	-3.49	77	20	1	2	3% p, 95% d	77	2	21
$2b_1$	-3.76	79	16	4	1	100% d	83	0	17
$4a_1$	-3.38	79	16	4	1	99% d	83	0	17
$1a_2$	-4.84	3	84	11	3		0	0	100
5e	-4.98	4	83	11	3		0	0	100
$3a_1$	-5.60	22	65	11	2	3% s, 89% d, 3% f	17	0	83
$4b_2$	-5.67	11	71	16	3	44% p, 41% d	4	5	91
4e	-5.78	17	67	14	2	11% p, 79% d, 6% f	10	1	89
$1b_1$	-6.08	24	62	12	2	97% d	17	0	83
3e	-6.72	33	63	0	4	41% p, 46% d, 4% f	13	11	76
$3b_2$	-6.81	41	56	0	3	13% p, 79% d, 5% f	25	3	72
$2a_1$	-7.46	33	64	0	3	74% s, 8% d, 12% f	32% 4s		66

(iii) Resonance PES. The line shapes of the CIS spectra in Figure 12a,b are due to resonance between the discrete absorption ($3p \rightarrow 3d$) and the continuum photoemission ($3d \rightarrow \epsilon\, 1$) channels as was originally described by Fano[54] for absorption spectroscopy. This formalism has been applied by Davis[11,12] to photoemission and is included in the CI model to generate the intensity expression given in eq 13. The term $(\epsilon + q)/(\epsilon + i)$ describes the intensity

$$I_n = \sigma_d\left[\alpha_n \cos\theta \frac{(\epsilon + q)}{(\epsilon + i)} - (\beta_n/\sqrt{2}) \sin\theta\right]^2 + \sigma_L[(\beta_n/\sqrt{2}) \cos\theta - \gamma_n \sin\theta]^2 \quad (13)$$

modulation of the d^8 final state caused by this resonance effect. Here, $\epsilon = (h\nu - h\nu_0)/\Gamma$, where $h\nu$ is the photon energy, $h\nu_0$ is the resonance energy, $2\Gamma = 2\pi V^2_{sck}$ is the SCK decay width (fwhm), and q is the Fano asymmetry parameter:

$$q = \frac{\langle 3d|\vec{r}|3p\rangle}{\pi V_{sck}\langle 3d|\vec{r}|\epsilon 1\rangle} \quad (14)$$

Since it is assumed that Auger decay from $3p^5\ 3d^{10}$ produces only the $|3d^8\rangle$ final state, only the first term ($\alpha_n \cos\theta$) in eq 13 is modified to include resonance effects. For $h\nu$ far from resonance, ϵ becomes large and eq 13 simplifies to eq 8.

This model of resonant intensity was applied to the final states in Figure 14a–c. For the ionic initial-state calculation, the $|d^8\rangle$ character resides in the lowest binding energy peak; thus only band A will show resonance at the absorption edge. Increasing T for the covalent ground-state calculation mixes $|d^8\rangle$ character into band B and both peaks will show resonance behavior. Finally, increasing U to a large value relative to Δ_1 for the relaxed final-state calculation shifts the resonance intensity from peak A into the satellite. This is qualitatively similar to the experimental data for $KCuCl_3$ and $(CH_3NH_3)_2CuCl_4$. The magnitude of the satellite resonant modulation predicted by the CI model (an increase in intensity of $^1\psi_3$ by a factor of 150 within this 10-eV range) is much greater than observed; however, the calculated ratio of the satellite to main band intensity modulation (28.4) is in reasonable agreement with experiment (22.4). The satellite CIS spectrum can be quantitatively reproduced using the wave functions of Table IX in eq 13 including two resonant profiles with an energy splitting of 2.6 eV (the Cu $3p^5$ spin–orbit splitting). In Figure 15 the accuracy of modeling the data indicates that an appropriate value of q (equal to 4.0) was chosen. Alternatively, the fit of the peak A CIS spectrum is not very good as the data clearly show two dips at approximately the same photon energies as the satellite CIS peaks (Figure 10), while the calculated d-band profile does not have this pronounced negative shape. The poor agreement with experiment again likely results from the adiabatic intensity approximation in eq 13.

(54) Fano, U. *Phys. Rev.* **1961**, *124*, 1866.

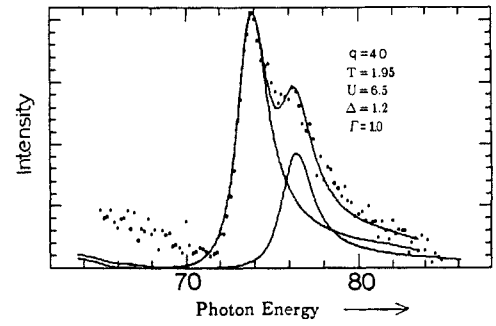

Figure 15. Comparison of the Configuration Interaction model calculated resonance profiles for $^1\psi_3$ and the experimental CIS spectrum of the satellite of $KCuCl_3$ assuming two resonance peaks split by 2.6 eV.

D. Comparison with D_{2d} $CuCl_4^{2-}$. In comparing the D_{2d} results with those for D_{4h} $CuCl_4^{2-}$, a number of quantitative differences were noted in the Results section which are summarized in Figure 8. The intensity ratio of peak A to B at the Cooper minimum is lower in the D_{2d} geometry qualitatively indicating that more d character is present in the ligand bonding levels, requiring an increase in covalent mixing. A two-Gaussian peak fit to the PES spectra for D_{2d} $CuCl_4^{2-}$ in Figure 7a gives experimental A/B intensity ratios of 1.15 (22 eV), 2.9 (48.4 eV), and 1.3 (1253.6 eV). Using eq 2 and $\sigma_{3p} = 0$, the decrease in the experimental peak intensity ratio at the Cooper minimum from 3.2 in D_{4h} to 2.9 in D_{2d} $CuCl_4^{2-}$ indicates that there is a 2% decrease in d character averaged over the metal antibonding levels. In addition, no low-energy peak C is observed and the satellite peak appears at 0.5 eV lower binding energy in the spectrum of the D_{2d} complex (Figure 8). The electronic structure changes responsible for these intensity and energy differences have been considered both through an SCF–Xα–SW calculation of D_{2d} $CuCl_4^{2-}$ ground state and through a CI calculation of the relaxed final states.

Table X presents the results of the Xα–SW calculations for the D_{2d} $CuCl_4^{2-}$ ground state using spheres adjusted to reproduce the experimental g values.[3b] The format of Table X corresponds to that of Table III.A for the D_{4h} complex. Comparison of these tables demonstrates that the $5b_2$ ($d_{x^2-y^2}$) highest energy half-occupied level of the D_{2d} structure is more ionic than the analogous $2b_{1g}$ orbital of D_{4h} $CuCl_4^{2-}$ (71 vs. 61% Cu d character). Alternatively, the covalent mixing averaged over the d orbitals is 3% greater in D_{2d}, indicating larger bonding interactions between orbitals of e, a_1, and b_1 symmetry. This increased average mixing results in a decrease in calculated A/B intensity ratio at the Cooper minimum [calculated D_{2d}, 3.19 (see supplementary material Table I), D_{4h} 3.88 (Table II.B.2], in agreement with the experimental trend.

The Xα–SW ground-state calculations in Table X also indicate that the energy splitting of the $5b_2$ and the next lower level (6e) is only 0.5 eV in D_{2d} $CuCl_4^{2-}$. The 0.5-eV splitting is much smaller

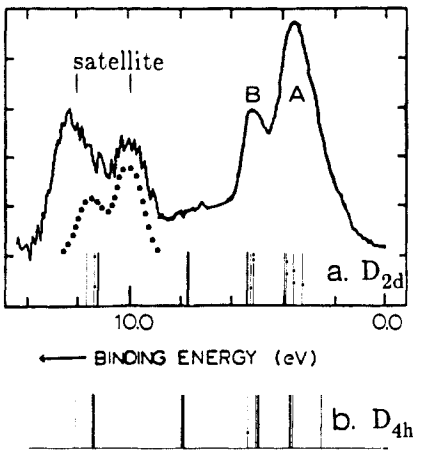

Figure 16. Comparison of composite Cs_2CuCl_4 PES spectrum with calculated Configuration Interaction energies for: (a) D_{2d} $CuCl_4^{2-}$ and (b) D_{4h} $CuCl_4^{2-}$. Portion of experimental spectrum showing peaks A and B taken at 48.4 eV, satellite region at 74 eV. The contribution from Cs 5p photoemission given by dotted peaks (···).

than the corresponding $3b_{1g}$–$2b_{2g}$ splitting of 1.5 eV in the D_{4h} $CuCl_4^{2-}$ ground-state calculation (Table III.A), consistent with the absence of a lower energy peak (C) in the D_{2d} spectrum. However, quantitative PES energy comparisons should include relaxation effects which are most easily considered with the CI model.

In application of the CI model to the valence band PES data for D_{2d} $CuCl_4^{2-}$, the values of U and Δ were fixed at those for D_{4h} $CuCl_4^{2-}$ (see section IV.B), and T_1 and T_2's were varied to fit the spectrum. A value of T_1 equal to 1.60 eV is required to reproduce the 0.5-eV smaller energy splitting of the satellite and main band peaks in D_{2d} $CuCl_4^{2-}$. This value of T_1 gives a ground-state $5b_2$ wave function with 67.7% Cu 3d character which parallels the Xα results, indicating that the ground-state wave function for D_{2d} $CuCl_4^{2-}$ is somewhat more ionic than that for the D_{4h} structure. Values for T_2 were estimated from the polarized single-crystal absorption spectrum[55] of Cs_2CuCl_4 and scaled by a factor of 0.737 so that the T_1 from optical data equals the 1.60 eV estimated from the PES spectrum. The values of T_2 used were 1.11 eV (e), 0.83 eV (b_1), and 0.71 eV (a_1) and are generally larger than those for the CI calculation of the D_{4h} complex. In agreement with experiment and the SCF–Xα–SW ground-state results, the CI orbital mixing averaged over the metal antibonding levels in D_{2d} $CuCl_4^{2-}$ (76% Cu 3d, 24% Cl 3p) is greater than that for D_{4h} $CuCl_4^{2-}$ (82% Cu 3d).

The CI calculated relaxed final-state energies for D_{2d} $CuCl_4^{2-}$ are compared with the composite PES spectrum and the results of the CI calculation for D_{4h} $CuCl_4^{2-}$ in Figure 16. These complexes clearly have a similar bonding description. The main quantitative energy differences between the D_{2d} and D_{4h} salts shown in Figure 16 are the lack of a distinct low-energy state corresponding to band C in D_{4h} spectra and the 0.5-eV decrease in the binding energy of the satellite peak. Both differences result from the reduced value of T_1 and thus reduced covalent mixing of the $d_{x^2-y^2}$ orbital in the D_{2d} geometry. The CI final-state wave functions for D_{2d} $CuCl_4^{2-}$ (given in supplementary material Table II) are quite similar to those found for D_{4h} $CuCl_4^{2-}$ with satellite states having 87% $|3d^8\rangle$ character and band A states having 66% $|d^9\underline{L}\rangle$ and 29% $|d^{10}\underline{L}^2\rangle$ consistent with the similarity in observed PES resonance effects.

V. Discussion

These variable-energy PES studies have provided detailed insight into the bonding in D_{4h} $CuCl_4^{2-}$. In particular, the fit of the CI model to the energy extremities of the valence band PES spectrum gives an estimate of the covalent mixing of the lowest energy $3b_{1g}$ orbital which is 65% Cu 3d character in the ground state. The value is compared with the results from a variety of other spectroscopic methods for the mixing of the half-occupied molecular orbital in Table XI. The values given in Table XI strongly support a $3b_{1g}$ ground state having 62 ± 5% $d_{x^2-y^2}$ character and indicate that photoelectron spectroscopy provides an estimate for this mixing in good agreement with the results from other spectroscopic methods. The intensity ratios of the PES peaks associated with metal antibonding and ligand bonding level ionizations at the ligand Cooper minimum reflect the metal character distributed over these levels. This ratio gives an experimental estimate of the covalent mixing averaged over all the d levels of 78% Cu 3d (for $\sigma_L = 0.00$), which is in good agreement with the results of ground-state Xα–SW calculations on D_{4h} $CuCl_4^{2-}$. The $2b_{2g}$, e_g, and $2a_{1g}$ levels have about 15% less mixing with the ligand orbitals, which is reasonable for D_{4h} $CuCl_4^{2-}$ in that the $d_{x^2-y^2}$ orbital lobes point directly at the four chloride ligands in the equatorial plane.

Table XI. D_{4h} $CuCl_4^{2-}$ Ground-State Covalent Mixing

	% Cu $d_{x^2-y^2}$ in ground-state wave function
ground state[a]	
g values—Xα adjusted	61
copper hyperfine	67
chlorine superhyperfine	64
excited state[b]	
d–d and CT energies—Configuration Interaction model	56
photoelectron spectra	
core level—XPS satellite[c]	60
valance level—variable-energy photoemission	65

[a] From ref 3a, 56 57. [b] From ref 53. [c] From ref 3b.

The absence of the low-energy peak C in the D_{2d} $CuCl_4^{2-}$ spectrum produces a CI fit that gives a covalent mixing of 68% Cu 3d for the lowest energy $5b_2$ level, a decrease of 3% relative to the $3b_{1g}$ level of the D_{4h} salt. This is consistent with the results of other spectroscopic methods which give a 5–10% decrease in the mixing of the half-occupied molecular orbital on comparing D_{4h} with D_{2d} $CuCl_4^{2-}$ (D_{2d} $CuCl_4^{2-}$: g values, 71% Cu 3d; hyperfine, 69%; superhyperfine, 75%; core level XPS, 64%).[3b,58] Alternatively, the D_{2d} metal to ligand peak intensity ratio (A/B) is 9% less than the D_{4h} ratio at the Cooper minimum, indicating that D_{2d} $CuCl_4^{2-}$ has a 2% increase in covalent mixing averaged over all the d levels. A distortion from the tetragonal to the tetrahedral geometry decreases the chloride overlap with the $d_{x^2-y^2}$ orbital, while ligand overlap with the remaining d levels is increased.

The PES spectrum of the valence band region of $CuCl_4^{2-}$ exhibits satellite peaks with ~10% of the intensity of the main ionization peaks at nonresonant photon energies. The Xα calculations allow an assignment of these satellite states as ligand ionization plus ligand to copper charge transfer shake-up transitions. In the frozen orbital approximation, these final states would correspond to two holes in dominantly ligand-centered molecular orbitals. However, the dominant resonance enhancement is observed in these satellite peaks, as also observed for NiO,[59] CuO,[6d] and transition metal chlorides.[60] Since the resonance is associated with the 3p → 3d absorption edge, the SCK Auger decay mechanism requires that these satellites have dominantly Cu $3d^8$ final-state character. Large orbital relaxation must occur and indeed, the final-state wave functions obtained from the relaxed Xα calculations do exhibit large increases in metal

(55) Ferguson, J. *J. Chem. Phys.* **1964**, *40*, 3406.
(56) Chow, C.; Chang, K.; Willet, R. D. *J. Chem. Phys.* **1973**, *59*, 2629.
(57) Thornley, J. H. M.; Mangum, B. W.; Griffiths, J. H. E.; Owen, J. *Proc. Phys. Soc. London* **1961**, *78*, 1263.
(58) Deeth, R. J.; Hitchman, M. A.; Lehmann, G.; Sachs, H. *Inorg. Chem.* **1984**, *23*, 1310.
(59) Oh, S.; Lindau, I.; Mikkelson, J. F. *Bull. Am. Phys. Soc.* **1981**, *26*, 461.
(60) Kakizaki, A.; Sugano, K.; Ishii, T.; Sugawara, H.; Nakagura, I.; Shin, S. *Phys. Rev. B* **1983**, *1026*.

character in the ionized ligand bonding levels. Insight into the electronic origin of this large relaxation can be obtained from the parameters derived from the CI model fit to the PES data. In particular, the loss of metal-centered electron–electron repulsion on going from the d^9 to the d^8 final-state configuration is much larger than the energy difference between metal and ligand valence bands (U = 6.5 as compared to Δ = 1.2 eV). It is this large metal-centered electron repulsion which strongly stabilizes the $|d^8\rangle$ final states.

Finally, it is important to note from Table IX (and experimentally demonstrated by the resonance photoemission data) that the wave function associated with the lowest energy final state of the ionized $CuCl_4^{2-}$ complex has dominantly $|d^9\underline{L}\rangle$ character, which corresponds to ligand ionization. However, a number of oxidized Cu(II)[61] and Ni(II)[62]) complexes have been prepared and have been assigned as having mostly $d^8(d^7)$ character in the ground state which corresponds to metal ionization. This must be the case for Ni(H_3-G_4) [where (H_3-G_4) is triply deprotonated tetraglycine] which has an odd number of electrons and has been studied by EPR spectroscopy. The complex has g_{av} values significantly greater than 2.00 with anisotropy ($g_\perp$ = 2.257, $g_\parallel$ = 2.010) indicating dominantly d_{z^2} character in a d^7 ground state.[62b] Further, Cu K-edge X-ray absorption spectroscopy of Cu(H_3-G_4) shows a large change in the spectrum with oxidation demonstrating that Cu(III) character must predominate.[63] Our analysis of the ionized $Cu^{II}Cl_4^{2-}$ complex can be extended to consider the factors which determine metal vs ligand oxidation for Cu(III) [and Ni(III)] complexes. As indicated above, ligand oxidation in the $CuCl_4^{2-}$ final state results from the 6.5-eV decrease in metal-centered electron–electron repulsion relative to the d^9 ground configuration upon ionization. In the CI formalism[64] in Figure 13, the d^8 final state configuration will be lowest in energy with a ligand (L) for which eq 15 is satisfied.

$$\Delta_L > U_{Cu\text{-}L} \tag{15}$$

This is clearly not the case for $CuCl_4^{2-}$ with $U_{Cu\text{-}Cl}$ = 6.5 eV and Δ_{Cl} = 1.2 eV.

To satisfy the $\Delta > U$ condition for a Cu(III) d^8 growth state, Δ must substantially increase and/or U must be lowered relative to the values obtained for $CuCl_4^{2-}$. The relative energy positions of the ligand bonding and metal d levels determine Δ; a ligand having a bonding level with a high ionization energy or a lowering of the Cu 3d level binding energy increases Δ, and thus will increase the d^8 final state character on ionization of a Cu(II) complex. PES spectra of the glycine molecule indicate that the nitrogen bonding levels are at significantly deeper binding energy than the Cl^- levels[65] (increasing Δ by at least 3 eV).

The metal centered electron repulsion, U, in a complex is substantially reduced from the free cupric ion value of >20 eV.[52a,66a] The reduced electron repulsion arises from nephelauxetic expansion of the metal d-orbitals resulting from decreased metal ion charge through covalent bonding interactions.[66] In this regard, the oxidation of Cu(II) precursors generally leads to Cu(III) complexes with a significant change in geometry to square planar with very short Cu–N bond lengths (~1.8 Å).[61] This would lead to substantial overlap of all bonding orbitals (metal 3d, 4s, and 4p), producing a larger covalent interaction and decreased electron repulsion. As a final note, this CI model does not include the effects of ligand repulsion, which would raise the energy of the $\underline{L}$ state and thus tend to stabilize a d^8 Cu(III) ground state. Most Cu(III) complexes are coordinated to second row atoms[61] (N, C, or O) and the L 2p levels should have larger repulsive interactions that the Cl^- 3p orbitals (U is ~4–5 eV greater for free 2nd row atoms).[67]

In summary, Cu(III) d^8 complexes should exist with 2nd row ligands having relatively large ionization energies which are still able to have strong covalent interactions with the metal ion.

Acknowledgment. We thank Kristine Butcher for useful discussions and help in the preparation of the manuscript. We acknowledge the Stanford Synchrotron Radiation Laboratory (SSRL) which is supported by the U.S. Department of Energy for providing beam time, the Stanford Center for Materials Research which is supported by the Division of Materials Research of the National Science Foundation for providing experimental facilities, and the National Science Foundation Grant CHE8613376 for financial support of this research.

Registry No. Cs_2CuCl_4, 35637-99-1; $(CH_3NH_3)_2CuCl_4$, 16950-47-3; $KCuCl_3$, 13877-25-3; Cu, 7440-50-8; CuCl, 7758-89-6; Cl_2, 7782-50-5.

Supplementary Material Available: Tables of Xα calculated ionization intensities from individual levels of D_{2d} $CuCl_4^{2-}$ and the CI calculated final-state wave functions for D_{2d} $CuCl_4^{2-}$ (2 pages). Ordering information is given on any current masthead page.

(61) (a) Bour, B. J.; Birker, P. J. M. W. L.; Steggerda, J. J. *Inorg. Chem.* **1971**, *10*, 1202. (b) Olson, D. C.; Vasilevskis, J. *Ibid.* **1971**, *10*, 463. (c) Beurskens, P. T.; Cras, J. A.; Steggerda, J. J. *Ibid.* **1967**, *7*, 811. (d) Allen, G. C.; Warren, K. D. *Ibid.* **1969**, *8*, 1895. (e) Margerum, D. W.; Chellappa, K. L.; Bossu, F. P.; Burce, G. L. *J. Am. Chem. Soc.* **1975**, *97*, 6894. (f) Bossu, F. P.; Chellappa, K. L.; Margerum, D. W. *Ibid.* **1977**, *99*, 2195. (g) Sharp, P. R.; Bard, A. J. *Inorg. Chem.* **1983**, *22*, 3462. (h) Castellani, C. B.; Fabbrizzi, L.; Liahelli, M.; Perotti, A.; Poggi, A. *J. Chem. Soc., Chem. Commun.* **1984**, 806.

(62) (a) Gore, E. S.; Busch, D. H. *Inorg. Chem.* **1973**, *12*, 1. (b) Lappin, A. G.; Murray, C. K.; Margerum, D. W. *Ibid.* **1978**, *17*, 1630. (c) Fabbrizzi, L.; Poggi, A. *J. Chem. Soc., Chem. Commun.* **1980**, 646. (d) Haines, R. I.; McAuley, A. *Inorg. Chem.* **1980**, *19*, 719.

(63) Blumberg, W. E.; Peisach, J.; Kosman, D. J.; Mason, H. S. *Oxidases Relat. Redox Syst., Proc. Int. Symp., 3rd 1979* **1982**, 1.

(64) Zaanen, J.; Sawatzky, G. A.; Allen, J. W. *Phys. Rev. Lett.* **1985**, *55*, 418.

(65) Cannington, P. H.; Ham, N. S. *J. Electron Spectrosc. Relat. Phenom.* **1984**, *34*, 327.

(66) (a) Brandow, B. H. *Adv. Phys.* **1977**, *26*, 651. (b) Wilson, J. A. *Ibid.* **1972**, *21*, 143.

(67) Harrison, W. A. *Phys. Rev. B* **1985**, *31*, 2121.